Ore Geology Reviews 95 (2018) 880–898

Contents lists available at ScienceDirect

Ore Geology Reviews

journal homepage: www.elsevier.com/locate/oregeorev

Age, origin and significance of the Wugang BIF in the Taihua complex, Southern North China Craton

Lei Liu[a,b], Huishan Zhang[c,d,*], Xiaoyong Yang[a,*], Yanguang Li[c,d]

[a] CAS Key Laboratory of Crust-Mantle Materials and Environments, School of Earth and Space Sciences, University of Science and Technology of China, 96 Jinzhai Road, Hefei 230026, China
[b] State Key Laboratory of Ore Deposit Geochemistry, Institute of Geochemistry, Chinese Academy of Sciences, Guiyang 550002, China
[c] MLR Key Laboratory for the Study of Focused Magmatism and Giant Ore Deposits, Xi'an, Center of Geological Survey, CGS, Xi'an 710054, China
[d] Center for Orogenic Belt Geology, Xi'an Center of Geological Survey, CGS, Xi'an 710054, China

ARTICLE INFO

Keywords:
Banded iron formation
Taihua complex
Neoarchean-Paleoproterozoic marine sediment
Zircon U-Pb dating
Wugang BIF

ABSTRACT

The Wugang BIF hosted in a Neoarchean Taihua complex (TH) in the Wugang area, at the southern margin of the North China Craton (NCC), is one of the important iron ore in Central Plain. In this study, we report new data on whole-rock compositions of iron ore sample, U-Pb isotopic compositions of detrital zircon from metasedimentary rocks (one BIF sample and two associated garnet parageneisses). In combination with literature data, they yielded a minimum age peak of 2.60 Ga for 110 detrital zircons of magmatic origin from the Tieshanmiao Formation (dominantly BIF-bearing strata) that we interpret as an upper limit age for the Wugang BIF depositional age. Thirty-six detrital zircons of metamorphic origin gave a maximum metamorphic age peak of 2.45 Ga, reflecting the lower limit age. Thus the depositional ages of Wugang BIF can constrained at 2.60–2.45 Ga. The presence of proximal detrital zircons in BIF samples, river-flux contributions, and some BIF samples have true negative Ce anomalies suggest that they were deposited in near-shore continental-shelf or back-arc basin environments, coinciding with that they are typically interbedded with marble, quartz arenite and other metasedimentary rocks, but lack of volcanic material. In particular, both hanging wall and footwall for Tiegukeng BIF orebody from Tieshanmiao Formation are marble, except for several diopside dykes (1943 Ma), orebody is dominantly composed of pyroxene-rich BIF, quartz-rich BIF and other metasedimentary rocks. The Wugang BIF displayed the weak positive $Eu/Eu^{*}_{(SN)}$ anomalies (average 1.74), associated with the low Cr (~10 ppm) and V (< 5 ppm) contents, similar to other Superior-type BIFs worldwide. All lines of evidence suggest that the Wugang BIF belongs to Superior-type. In combination with features of coeval counterpart, such as Huoqiu BIF and Xincai BIF in its southeast, it can be assumed that a relatively large Superior-type BIF belt presented at proto-continental margin, they deposited on proto-continental shelf or back-arc basin environments during Neoarchean-Paleoproterozoic. Geochemical evidence propose that the Wugang BIF originated from chemical deposition of carbonate and silica facies, its iron sourced from the mixture of seawater, hydrothermal fluid and river-flux, with trace continental detritus. Consequently, it is reasonable to predict that a great variety of BIFs may distribute between Wugang and Huoqiu area at the southern margin of NCC.

1. Introduction

As a common chemical sediment in Precambrian Earth, Banded iron formations (BIFs) are closely associated with greenstone belts and supracrustal sequences (e.g., James, 1992; Zhai and Santosh, 2011, 2013). It is now generally accepted that BIFs are economically important iron sources in the world, and the related researches provide important constraints on paleoceanographic variability, geochemical evolution of early Earth (Klein, 2005; Bekker et al., 2010; Schimmelmann et al., 2016). Therefore, studies on BIFs is invaluable both in economical and geoscientific fields. As a faithful record, Precambrian BIFs reflect secular changes in the geological history and metallogenic epochs of an evolving Earth (Zhai and Santosh, 2013).

A great variety of BIFs was deposited in some greenstone-belts areas of the NCC, such as Anshan-Benxi, eastern Hebei, Wutai and western Shandong, helping to establish a window to documenting the paleoceanographic and environmental evolution (Zhang et al., 2012). BIFs in the northern NCC have a wide range in their formation ages, yet the peak period is 2.56–2.52 Ga, and is dominantly composed of Algoma-type. However, recent researches pointed out some 2.7–2.5 Ga BIFs

* Corresponding authors at: MLR Key Laboratory for the Study of Focused Magmatism and Giant Ore Deposits, Xi'an, Center of Geological Survey, CGS, Xi'an 710054, China (H. Zhang).
E-mail addresses: zhanghuishan.2086@163.com (H. Zhang), xyyang@ustc.edu.cn (X. Yang).

https://doi.org/10.1016/j.oregeorev.2018.04.005
Received 25 August 2017; Received in revised form 30 March 2018; Accepted 3 April 2018
Available online 04 April 2018
0169-1368/

from the southern and eastern NCC have typical characteristics similar to Superior-type BIF, such as Huoqiu, Xincai and Changyi BIFs (Lan et al., 2014, 2017a; Wang et al., 2015; Liu and Yang, 2015). The significant differences they have are included in formation ages, depositional types and environments, and source features. However, researches on BIFs in southern NCC are weaker than those from northern NCC. Thus it is necessary to amplify the investigation on BIFs from southern NCC, in order to provide more comparisons between BIFs in southern and northern NCC, and theoretical predictions for BIF exploration in southern NCC.

The Taihua complex is located at the southern NCC, is mainly composed of a series of early Precambrian medium-high grade metamorphic rocks, including TTG gneisses, amphibolites, supracrustal rocks and so forth. BIFs are mainly distributed in Wugang and Lushan areas within Taihua complex. The proven reserves for BIF iron deposits is more than 600 million tons in Wugang area, whereas less than 100 million tons in Lushan area. Therefore, we chose the represented BIF from Wugang area as the investigated target, such as Tieshanmiao, Jingshansi and Tiegukeng mining areas. It is worth to note that there presents another type of iron deposit in this area, Zhaoanzhuang-type iron deposit, which does not belong to BIF, but akin to magmatic iron deposit. For better distinguish each other, the BIF in Wugang area has been named as Tieshanmiao-type by previous geologists. In this study, we focus on the Tieshanmiao-type iron deposits or the Wugang BIF.

Previous studies from whole-rock and mineral chemistry suggested that the Wugang BIF deposited in an anoxic marine environment, and was sourced from mixing of seawater with high-T hydrothermal fluids without any continental detritus contamination (Lan et al., 2013, 2017b; Yao et al., 2015). Evidence from mineralogical and microfabric characteristics of magnetite indicated that the depositional environments for two sub-types of quartz-magnetite BIFs (Q-BIF) and pyroxene-magnetite BIFs (P-BIF) were different, the former was deposited at the long-term interval of volcanic eruptions, and the magnetite crystalized under oxygen fugacity (fO_2) fluctuated conditions; whereas the latter was affected by the volcanic eruption, and the magnetite formed in a steady fO_2 setting (Li et al., 2014). Yao et al. (2015) proposed both subtypes represent metamorphosed quartz-carbonate iron-bearing formations according to their geological and geochemical characteristics. The positive correlation between CaO and SiO_2, MgO and SiO_2 of the P-BIF corresponds with the occurrence of pyroxene, indicating a metamorphic origin for pyroxene instead of magmatic origin (Yao et al., 2015). However, the formation time, tectonic setting and deposition environment of the Wugang BIF are poorly known. Furthermore, comparisons with nearby Huoqiu and Xincai BIFs, and comparisons between BIFs in southern and northern NCC have no report so far. In order to gain new insights into this early Precambrian chemical sedimentary iron deposit, in particular, its metallogenic significance in southern NCC, we carried out this study, covering newly acquired geochronological and geochemical data directly from BIF samples and their associated metasedimentary rocks using current state-of-the-art analytical methods. Coupled with previously reported data, it becomes clear that the Wugang BIF shared some key features with Huoqiu and Xincai BIFs, implying that a large BIF metalliferous belt distributes along southern margin of NCC.

2. Geological setting

As the oldest and largest craton in China, the North China Craton (NCC) has been intensively investigated due to complex evolution that includes removal of its deep cratonic mantle root, muti-episodes continental crustal growth events during Mesoarchean-Neoarchean and abundant mineral resources (Zhao and Zhai, 2013; Zhai and Santosh, 2013 and references therein). The NCC has been tectonically divided into two Blocks of Eastern and Western by the Trans-North China Orogen (TNCO), based on their lithological, structural, metamorphic and geochronological differences (Fig. 1a; Zhao et al., 2005; Huang et al., 2010). The TNCO represents a major Paleoproterozoic subduction-collision belt between the Eastern and Western Blocks, actually, many Neoarchean terranes are exposed in the southern part of the TNCO such as the Dengfeng, Zhongtiao and the Taihua complexes (Liu et al., 2009; Wan et al., 2009; Huang et al., 2010; Zhang et al., 2014).

The Taihua complex (TH) was discretely exposed at the southern margin of the NS-striking TNCO, which predominantly consists of Huashan, Xiaoshan, Luoning, Lushan and Wugang Neoarchean blocks from northwest to southeast (Fig. 1a). Based on new geological and geochronological studies, the Taihua Group can be divided into Paleoproterozoic Upper Taihua Group and Neoarchean Lower Taihua Group (also named as Taihua complex (TH)). In terms of geochronological studies on TTG rocks and plagioclase amphibolites from Lushan block, it is suggested that TH was formed during Early Neoarchean (Diwu et al., 2010; Huang et al., 2010). As a whole, TH experienced quite similar metamorphic process such as clockwise P-T paths occurred at 1.96–1.80 Ga (Lu et al., 2014 and references therein).

The Wugang block (local place name changed from "Wuyang" to "Wugang" in 1990, thus Wuyang is often used in previous references) is located at the easternmost part of TH, which presents abundant iron ore source, including mainly of two types iron ore, Tieshanmiao-type BIF and Zhaoanzhuang-type magmatic origin iron ore (Fig. 1b). Where the former ore deposits are characteristic of large reserve more than 600 million tons with an average total Fe grade of 25–29 wt%, yet the latter one has relative high total Fe grade (approximately 40 wt%), but its reserve is no more than 100 million tons. TH exposed in this block is subdivided into three Formations, from bottom to top, Zhaoanzhuang Formation (ZAZ), Tieshanmiao Formation (TSM), and Yangshuwan Formation (YSW). Tieshanmiao-type BIF deposits and Zhaoanzhuang-type magmatic origin iron deposits are distributed in TSM and ZAZ, respectively (Fig. 1c). Both types of iron deposit have received widespread attention due to they have contrasting geochemical and mineralogical characteristics. The Zhaoanzhuang-type iron deposit is closely related to the ultramafic rocks both spatially and temporally, and they share similar mineral assemblages and compositions, indicating a magmatic origin (Lan et al., 2015); whereas the Tieshanmiao-type iron deposit belongs to banded iron formation as a result of their major compositions (e.g., very low contents of Al_2O_3, TiO_2 and NiO) and trace compositions (they have similar REE + Y patterns with characteristics of modern seawater and hydrothermal fluids) (Lan et al., 2013, 2017b; Yao et al., 2015). The widespread of migmatites in this unit indicates that the Wugang block had experienced upper amphibolite to granulite facies metamorphism (Lu et al., 2014).

In this study, we focus on the Tieshanmiao-type BIF deposits, which are distributed in Jingshansi, Tiegukeng (Tieshan) and Tieshanmiao mining areas along NW-SE direction (Fig. 1b). TSM is mainly composed of banded migmatite, amphibole gneiss and minor quartzite and marble (Fig. 1c). Ore strata C and D have 300 m and 200 m in depth, respectively, which are interbedded with banded migmatite, plagioclase amphibole gneiss and quartzite (Fig. 1c). Last but not least, field observations suggest both hanging wall and footwall for Tiegukeng iron orebody are marble (Fig. 2a).

3. Samples description

Two types of iron ores have be collected from Jingshansi and Tiegukeng mining areas (Fig. 1b). One type is banded quartz-rich iron formation (Q-BIF), the other type is pyroxene-rich massive magnetite ore, which is also metamorphosed from BIF (P-BIF, Li et al., 2014; Yao et al., 2015). In this region, despite suffering upper amphibolite facies metamorphism (Lu et al., 2014), the banding is well preserved in Q-BIF. The fine-grained band is less than 1 mm wide, whereas the coarse-grained band is more than 2 mm wide (Yao et al., 2015). According to the scales of banding, these samples displayed features of microbanding and mesobanding, respectively (Trendall and Blockley, 1970). Samples 14WG-21 to -30 are derived from Tiegukeng ore deposit (Fig. 2a),

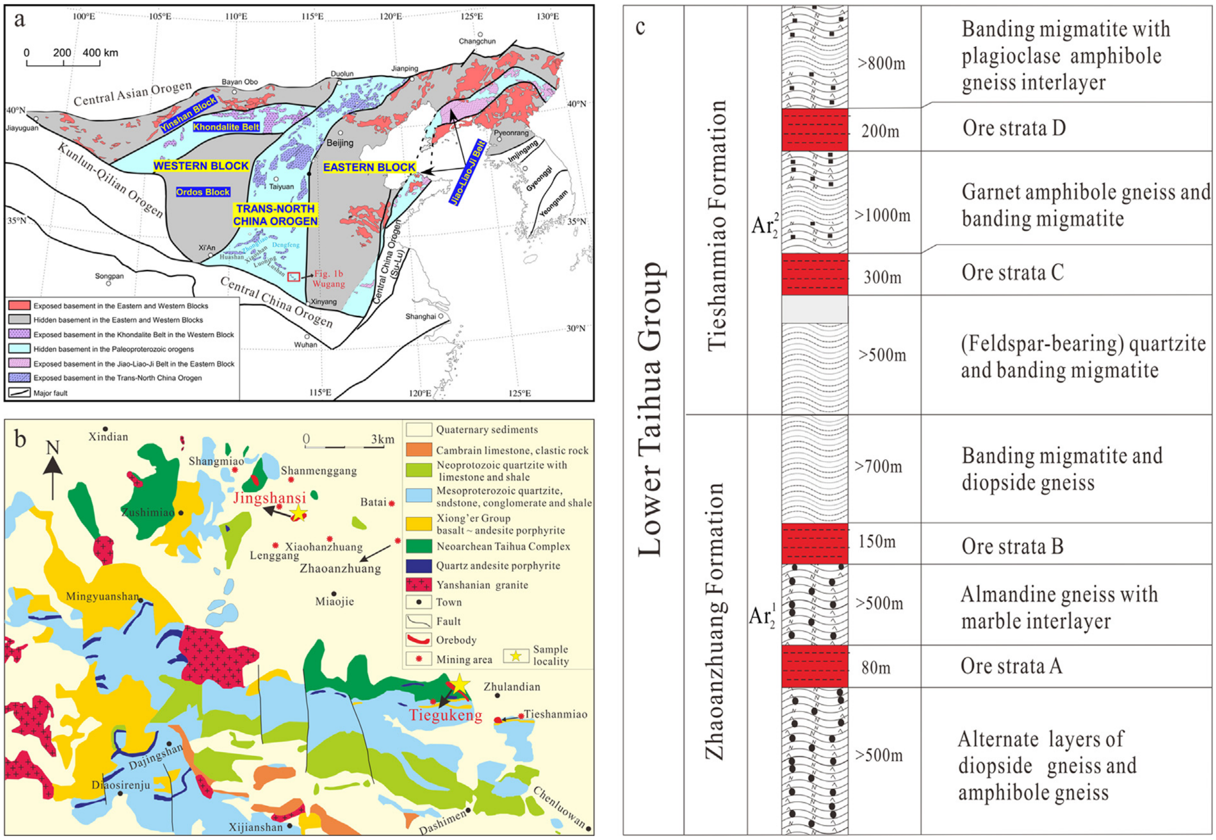

Fig. 1. (a) Geologic and tectonic map of the NCC (modified from Zhao et al., 2005). Two blocks, one major Trans-North China Orogen and three subordinate accretionary belts are shown; (b) Simplified geological map of the Wugang terrane (modified after Lan et al., 2013; Li et al., 2014). In this map, most of the Wugang region is covered by Quaternary sediments, Proterozoic, Cambrian and Eogene strata are sporadically exposed in the southern and western parts. Samples in this study are dominantly from Tiegukeng and Jingshansi deposits, both belong to Tieshanmiao Formation (TSM); (c) General rock strata column of the Taihua complex (TH) after Li et al. (2014). Iron ore strata A and B belong to Zhaoanzhuang Formation (ZAZ), whereas C and D belong to TSM.

which made up a profile passing through the orebody core. The average distances between two samples are 2–3 m. Two types of iron ores display distinct features in hand specimen and photomicrograph (Fig. 2b–e). The Q-BIF shows continuous stratigraphic micro-bands of quartz, whereas the P-BIF do not display any bands, but disseminated and massive structure (Fig. 2c). The bands of Q-BIF are mainly composed of alternating pyroxene-magnetite-rich bands and quartz-rich bands (Fig. 2d), yet pyroxene (approximately 60%) and magnetite (approximately 40%) made up the P-BIF (Fig. 2e). Some newly grown quartz bands occasionally occur in the white bands with similar lateral extension (Fig. 2d; Yao et al., 2015).

In addition to abovementioned ten ore samples, the reminding samples are collected from Jingshansi deposit, including four BIFs and two garnet gneisses. Two garnet gneisses (14WG-36 and 14WG-37) are mainly composed of plagioclase, quartz, and biotite, with minor scattered garnet, belong to Al-rich paragneiss. Their protoliths are dominated by sediment and minor volcanoclastic rock and tuff. Due to they occurred in association with orebody, they were dated together with BIF sample 14WG-3.

4. Analytical methods

4.1. Whole-rock major and trace element analysis

Fourteen BIF samples and two garnet gneisses were crushed in steel jaw crushers and then powdered using an agate mill to grain sizes < 200 mesh at ALS Geochemistry Laboratory in Guangzhou, Guangdong Province. Major oxides analyses were performed by wavelength-dispersive X-ray fluorescence spectrometry (XRF) on fused glass beads using an AXIOS Minerals spectrometer at ALS, with the analytical uncertainties less than 1% RSD. Loss of ignition (LOI) was determined by igniting a sample powder at 1000 °C for one hour. The negative values for LOI are result of FeO oxidized into Fe_2O_3 under air circumstance. Trace and rare earth elements were determined by high resolution inductively coupled plasma mass spectrometer (ICP-MS) of solutions on an Elan DRC-II instrument at ALS. 50 mg powders were precisely weighted and dissolved in closed beakers, after 2-day digestion under a mixture of HF and HNO_3 acids in Teflon screw-cap bombs. The error is estimated to be better than 5% for all elements by this measured method.

4.2. Zircon U-Pb dating and trace elements

Zircons from one BIF sample and two associated garnet gneisses (14WG-36, 14WG-37 and 14WG-3) are selected for U-Pb isotopic analyses. Zircon crystal grains were separated using the magnetic-gravimetric techniques, with hand-picking under a binocular microscope. Then zircon grains were mounted on an epoxy disk and polished until their cores were exposed. Cathodoluminescence (CL) images were made by microprobe JEOL JXA-8100 electron microanalyses at Chinese Academy of Sciences (CAS) key Laboratory of Crust-Mantle Materials and Environments in University of Science and Technology of China (USTC), Hefei, Anhui Province. Zircon U-Pb dating and trace element analyses were determined at above-mentioned laboratory, using an Agilent 7500 quadruple-ICP-MS equipped with a 193 nm excimer ArF laser-ablation system. Zircon standard 91,500 was used to adjust instrument drift and mass bias correction during unknown analyses. The correction factors for the $^{207}Pb/^{206}Pb$ ratio were calculated using

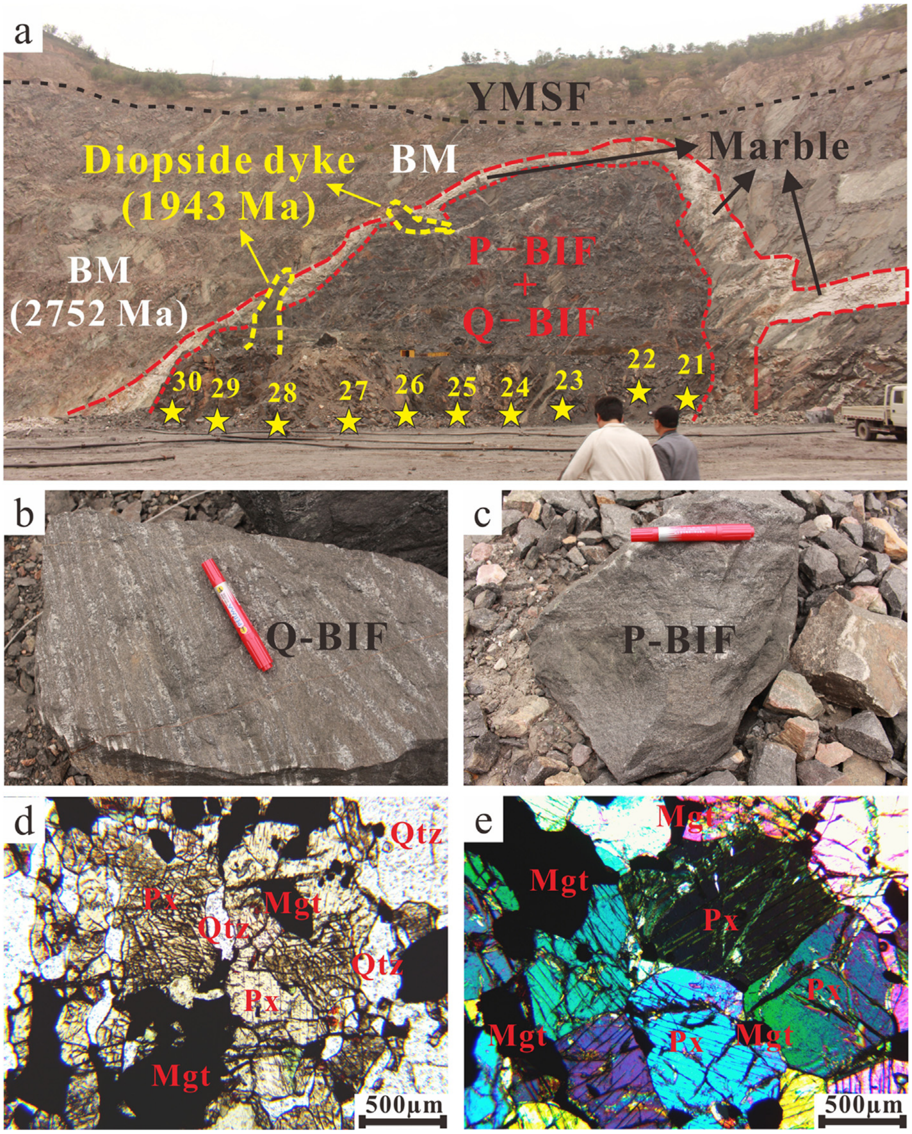

Fig. 2. (a) Field photograph of Tiegukeng ore deposit; diopside dyke cutting marble and BIF layer have been shown, where the emplacement age of the dyke was constrained at 1943 Ma by Zhang et al. (2016), and the formation age of banded migmatite (BM) was 2752 Ma (Diwu et al., 2010). It is worth to note that both hanging wall and footwall for BIF orebody are marble. The Mesoproterozoic covered layer, Yunmengshan Formation (YMSF) has also shown; (b and c) two represented hand specimens for quartz-rich BIF (Q-BIF) and pyroxene-rich BIF (P-BIF); and their corresponding photomicrographs (d and e). Yellow number 21–30 denote the localities of sample 14WG-21 to -30, respectively. (For interpretation of the references to colour in this figure legend, the reader is referred to the web version of this article.)

analyses of NIST 610, analyzed throughout the day and calculated using the recommended values by Baker et al. (2004). NIST 612 is the external standard for calibration of trace elements. Every 5 unknowns was bracketed by once standard analyses. The time for unknown analysis is 30 s, followed by 20 s blank analysis. Helium gas was used as the carrier gas to enhance the transport efficiency. Then the carrier gas was mixed with argon inside the ablation cell before entering the ICP for analysis. A laser beam size of 32–44 μm in diameter was applied at a repetition rate of 5 Hz and an energy density of 2 J/cm^2. The detailed operating procedures have been described by Liu et al. (2007). The data were dealt with the ISOPLOT program of Ludwig (2003).

4.3. Zircon Hf isotopes

Zircon in-situ Lu-Hf analyses were conducted using a Nu Plusma HR MC-ICPMS (Nu Instruments Ltd., UK) equipped with a Geolas 2005 193 nm ArF-excimer laser-ablation system at the State Key Laboratory of Continental Dynamics, Northwest University, Xi'an, China. The laser beam of 44 μm in diameter with a repetition rate of 8 Hz, and an energy density of 10 J/cm^{-2} were applied in this study. He gas used as carrier gas. The instrumental conditions and data acquisition were described in detailed by Yuan et al. (2008). The corrections to raw Lu-Hf isotopic data followed the protocols of Yuan et al. (2008). Correction for isobaric interference of ^{176}Lu on ^{176}Hf and ^{176}Yb on ^{176}Hf was using the recommended ^{176}Lu/^{175}Lu ratio of 0.02655 (Machado and Simonetti, 2001) and ^{176}Yb/^{172}Yb ratio of 0.5886 (Chu et al., 2002), respectively. Harvard zircon 91500, Monastery and GJ-1 were used as references during analyses. All the Lu-Hf isotopic results are reported in 2σ error. A decay constant for ^{176}Lu of 1.865×10^{-11} a^{-1} (Scherer et al., 2001), the present-day chondritic ratios of ^{176}Hf/^{177}Hf = 0.282772 and ^{176}Lu/^{177}Hf = 0.0332 (Blichert-Toft and Albarede, 1997) were applied in calculate ε_{Hf}(t) values. Hf model ages (t_{DM1}) were calculated relative to the depleted mantle present-day values of ^{176}Hf/^{177}Hf = 0.28325 (Nowell et al., 1998) and ^{176}Lu/^{177}Hf = 0.0384 (Griffin et al., 2000). Crustal model ages (t_{DM2}) were obtained by assuming that the parental magma was produced from average continental crustal (^{176}Lu/^{177}Hf = 0.015). The Lu-Hf analysis used the same mounts and same sites as those for U-Pb dating in most cases, when this was not possible, the adjacent site within the same zircon grain was analyzed.

5. Results

5.1. Whole-rock major and trace elements

Fourteen ore samples and two associated paragneisses were analyzed for major and trace elements and the results are listed in Table 1.

Table 1
Major (wt.%) and trace element (ppm) compositions of whole rocks for BIFs and paragneisses (PG) from Tieshanmiao formation.

Sample	14WG-21	14WG-22	14WG-23	14WG-24	14WG-25	14WG-26	14WG-27	14WG-28	14WG-29	14WG-30	14WG-3	14WG-32	14WG-33	14WG-35	14WG-36	14WG-37
Rock-type	P-BIF	P-BIF	Q-BIF	Q-BIF	Q-BIF	P-BIF	P-BIF	Q-BIF	Q-BIF	Q-BIF	P-BIF	Q-BIF	Q-BIF	P-BIF	PG	PG
Unit	TSM	TSM	TSM	TSM	TSM	TSM	TSM	TSM	TSM	TSM	TSM	TSM	TSM	TSM	TSM	TSM
SiO_2	45.17	52.20	49.83	48.46	41.46	42.16	41.66	52.51	45.38	50.54	40.32	46.29	45.67	38.18	63.54	65.31
Al_2O_3	0.21	0.13	0.23	0.63	0.59	0.41	0.10	0.15	0.24	0.25	0.67	0.37	0.29	0.46	15.67	14.59
Fe_2O_3	29.99	39.09	41.63	40.26	47.84	47.16	53.79	38.80	47.60	42.52	42.27	47.54	46.67	43.13	6.62	5.86
MgO	5.01	2.72	4.30	4.84	3.07	3.38	2.09	2.33	2.78	2.88	5.31	2.20	2.43	5.84	2.73	4.08
CaO	18.92	5.49	4.07	5.01	6.49	6.04	2.49	4.10	3.91	4.00	9.88	3.87	4.09	10.86	4.60	1.27
Na_2O	0.73	0.38	0.27	0.50	0.69	1.43	0.39	0.40	0.50	0.57	1.49	0.48	0.54	1.73	1.17	4.03
K_2O	0.02	0.02	0.04	0.20	0.19	0.01	0.06	0.01	0.01	0.01	0.53	0.01	0.02	0.02	2.63	2.53
TiO_2	< 0.01	< 0.01	< 0.01	< 0.01	< 0.01	< 0.01	< 0.01	< 0.01	< 0.01	< 0.01	< 0.01	< 0.01	< 0.01	< 0.01	0.61	0.64
MnO	0.28	0.15	0.23	0.28	0.27	0.20	0.14	0.17	0.16	0.11	0.29	0.14	0.15	0.31	0.16	0.05
Cr_2O_3	0.01	0.01	0.01	0.01	0.01	0.01	0.01	0.01	0.01	0.01	0.01	0.01	0.01	0.01	0.01	0.04
BaO	0.01	0.01	0.01	0.01	0.01	0.01	0.01	0.01	0.01	0.01	0.01	0.01	0.01	0.01	0.03	0.03
P_2O_5	0.028	0.031	0.017	0.025	0.006	0.004	0.002	< 0.001	0.016	0.027	0.002	0.011	0.015	0.003	0.132	0.079
SrO	0.01	0.01	0.01	0.01	0.02	0.02	0.01	0.01	0.01	0.01	0.01	0.01	0.01	0.01	0.01	0.01
LOI	−0.35	−0.98	−1.03	−0.18	−1.04	−1.08	−0.97	0.67	−0.96	−0.96	−0.81	−0.40	−0.36	−0.27	2.35	1.00
Total	100.04	99.26	99.62	100.06	99.61	99.75	99.78	99.17	99.67	99.98	99.98	100.54	99.55	100.29	100.26	99.52
Ba	2.4	2.2	3.3	3.7	11.1	0.9	1.0	1.4	0.7	0.5	5.0	1.2	1.4	1.6	324	259
Zr	2	2	18	4	2	< 2	< 2	< 2	< 2	< 2	4	6	6	< 2	165	255
Cr	10	10	20	10	10	10	20	20	10	10	20	20	20	10	50	290
Cs	0.19	0.06	0.43	1.38	0.15	0.09	0.11	0.15	0.09	0.14	2.50	0.07	0.08	0.11	3.09	3.74
Ga	0.9	0.5	0.7	1.3	1.3	0.9	0.9	0.7	1.0	0.7	1.2	1.1	1.0	2.6	19.1	18.7
Rb	0.6	0.4	2.6	22.1	9.4	0.2	0.2	0.4	0.2	0.2	52.1	0.2	0.2	0.3	111.5	96.6
Sn	1	< 1	< 1	< 1	< 1	< 1	1	< 1	< 1	< 1	1	1	< 1	2	1	1
Sr	26.4	32.1	25.3	14.7	75.6	102.5	20.6	60.7	54.0	65.6	18.3	32.8	40.5	59.2	123.5	56.3
Hf	< 0.2	< 0.2	0.5	0.2	0.2	< 0.2	< 0.2	< 0.2	< 0.2	< 0.2	< 0.2	0.3	0.3	< 0.2	4.1	6.7
V	< 5	< 5	< 5	< 5	< 5	< 5	< 5	< 5	< 5	< 5	< 5	< 5	< 5	15	97	99
Nb	0.7	< 0.2	0.4	0.2	0.3	< 0.2	0.7	< 0.2	0.2	< 0.2	0.4	1.1	0.8	1.0	6.7	8.0
Ta	0.3	< 0.1	< 0.1	< 0.1	< 0.1	< 0.1	0.2	< 0.1	< 0.1	< 0.1	< 0.1	0.2	< 0.1	0.6	0.5	0.7
Th	0.13	0.09	0.23	0.16	0.20	0.16	0.14	0.08	0.10	0.16	0.31	0.09	0.12	0.17	3.78	7.52
U	0.07	0.09	0.14	0.12	< 0.05	0.09	0.09	0.05	0.07	< 0.05	0.25	0.07	0.05	0.10	0.46	1.85
La	0.7	1.1	1.0	1.1	1.1	0.8	< 0.5	0.7	1.0	1.3	1.5	0.8	1.1	0.9	22.5	24.4
Ce	1.2	2.1	2.1	2.1	2.2	1.4	0.6	1.2	1.8	2.1	3.5	1.4	1.7	2.2	44.8	47.9
Pr	0.14	0.26	0.25	0.27	0.23	0.18	0.07	0.14	0.22	0.24	0.39	0.14	0.17	0.29	4.94	5.40
Nd	0.6	1.1	1.2	1.0	1.1	0.7	0.3	0.6	0.9	1.2	1.4	0.6	0.6	1.1	20.0	20.0
Sm	0.16	0.29	0.29	0.26	0.19	0.09	0.08	0.09	0.26	0.21	0.20	0.16	0.14	0.32	3.46	3.72
Eu	0.05	0.07	0.13	0.07	0.06	0.05	0.03	0.06	0.09	0.12	0.07	0.04	0.05	0.14	1.18	0.90
Gd	0.18	0.22	0.29	0.19	0.20	0.16	0.09	0.18	0.20	0.21	0.22	0.14	0.13	0.33	3.08	3.52
Tb	0.03	0.02	0.04	0.03	0.02	0.02	0.02	0.03	0.04	0.04	0.03	0.02	0.02	0.06	0.48	0.55
Dy	0.14	0.24	0.26	0.16	0.14	0.17	0.07	0.18	0.26	0.35	0.28	0.14	0.13	0.35	3.00	3.38
Y	1.6	2.5	3.2	1.8	1.7	2.1	1.5	2.4	3.3	3.6	2.1	1.8	1.9	2.9	15.7	19.3
Ho	0.04	0.07	0.08	0.04	0.04	0.04	0.03	0.05	0.07	0.07	0.06	0.04	0.04	0.10	0.56	0.74
Er	0.12	0.17	0.25	0.16	0.13	0.17	0.12	0.19	0.26	0.26	0.13	0.12	0.13	0.25	1.53	2.15
Tm	0.02	0.03	0.03	0.02	0.01	0.03	0.02	0.02	0.04	0.04	0.02	0.02	0.02	0.03	0.22	0.31
Yb	0.09	0.18	0.26	0.16	0.14	0.11	0.16	0.19	0.24	0.29	0.21	0.09	0.14	0.22	1.70	2.03
Lu	0.02	0.03	0.04	0.03	0.02	0.03	0.02	0.02	0.05	0.04	0.03	0.03	0.04	0.06	0.25	0.33
ΣREE	5.09	8.38	9.42	7.39	7.28	6.05	3.61	6.05	8.73	10.07	10.14	5.54	6.31	9.25		
$Y/Y^*_{(SN)}$	1.69	1.52	1.74	1.79	1.79	2.03	2.46	2.00	1.94	1.83	1.29	1.90	2.07	1.22		
$La/La^*_{(SN)}$	1.51	1.23	1.85	0.88	2.17	1.05	2.15	1.51	1.21	3.17	0.79	1.72	1.29	0.70		
$Ce/Ce^*_{(SN)}$	0.88	0.91	0.97	0.89	1.01	0.85	0.72	0.88	0.89	0.86	1.05	0.96	0.89	0.98		
$Pr/Pr^*_{(SN)}$	0.97	1.00	0.92	1.09	0.87	1.07	0.97	0.97	1.01	0.88	1.04	0.90	0.99	1.09		
$Eu/Eu^*_{(SN)}$	1.37	1.30	2.10	1.48	1.44	1.83	1.65	2.03	1.86	2.68	1.56	1.26	1.74	2.02		
$Gd/Gd^*_{(SN)}$	0.81	118.76	1.30	0.94	1.97	2.24	0.53	0.99	0.90	1.58	2.67	1.38	1.17	0.88		
$Sm/Yb_{(SN)}$	0.90	0.82	0.57	0.83	0.69	0.42	0.25	0.24	0.55	0.37	0.48	0.90	0.51	0.74		

(continued on next page)

Table 1 (*continued*)

Sample	14WG-21	14WG-22	14WG-23	14WG-24	14WG-25	14WG-26	14WG-27	14WG-28	14WG-29	14WG-30	14WG-3	14WG-32	14WG-33	14WG-35	14WG-36	14WG-37
Rock-type	P-BIF	P-BIF	Q-BIF	Q-BIF	Q-BIF	P-BIF	P-BIF	Q-BIF	Q-BIF	Q-BIF	P-BIF	Q-BIF	Q-BIF	P-BIF	PG	PG
Unit	TSM	TSM	TSM	TSM	TSM	TSM	TSM	TSM	TSM	TSM	TSM	TSM	TSM	TSM	TSM	TSM
$Pr/Yb_{(SN)}$	0.50	0.46	0.31	0.54	0.52	0.52	0.14	0.24	0.29	0.26	0.59	0.50	0.39	0.42		
$La/Yb_{(SN)}$	0.57	0.45	0.28	0.51	0.58	0.54	0.23	0.27	0.31	0.33	0.53	0.66	0.58	0.30		
Y/Ho	40	36	40	45	43	53	50	48	47	51	35	45	48	29		
Eu/Sm	0.31	0.24	0.45	0.27	0.32	0.56	0.38	0.67	0.35	0.57	0.35	0.25	0.36	0.44		
Sm/Yb	1.78	1.61	1.12	1.63	1.36	0.82	0.50	0.47	1.08	0.72	0.95	1.78	1.00	1.45		
Ce/Yb	13.33	11.67	8.08	13.13	15.71	12.73	3.75	6.32	7.50	7.24	16.67	15.56	12.14	10.00		

SN means normalization to PAAS values after McLennan (1989).

Ore samples contained P-BIF and Q-BIF. They are characteristic by high SiO_2 (45.7 wt% in average) and Fe_2O_3 (43.5 wt% in average) in composition, and P-BIF display higher CaO and MgO contents than those in Q-BIF. Both TiO_2 and Al_2O_3 contents are very low in these ore samples, in particular for TiO_2, almost < 0.01 wt%. MnO, Cr_2O_3, BaO and P_2O_5 also have very low contents in ore samples (most < 0.01 wt%). Two paragneisses have high SiO_2 (63.5–65.3 wt%) and medium Al_2O_3 (14.6–15.7 wt%) in compositions. They share similar Fe_2O_3 + MgO contents and CaO + Na_2O + K_2O contents. Sample 14WG-36 has higher CaO than those in sample 14WG-37. By contrast, it has lower Na_2O than those in sample 14WG-37, which is consistent with albite and anorthite distribution in photomicrograph.

The trace and rare earth element (REE) compositions of five P-BIF samples and eight Q-BIF samples from the Tieshanmiao-type iron deposits are presented in Table 1 and Fig. 3. Since Y is an element geochemically similar to the heavy rare earth element (HREE) Ho, but displays different complexation properties in marine systems (Ho is scavenged on particulate matter two times faster than Y) (Nozaki et al., 1997), here we use REE + Y (REY) compositions of BIF to elucidate the features of these sedimentary rocks. The REY for all ore samples are normalized by the Post Archean Australian Shale (PAAS, McLennan, 1989). Both P-BIF and Q-BIF display significant positive Eu and Y anomalies, and show depletion towards LREY (Fig. 3), and in general, LREY are slightly more depleted than MREY and HREY (Fig. 4). The Eu anomalies are recorded by $Eu/Eu^*_{(SN)}$ (footnote SN means normalized to those of PAAS). In this study, the values of all BIF samples fall in the range between 1.26 and 2.68 with an average of 1.74. The positive Y anomalies are expressed as $Y/Y^*_{(SN)}$, and their values range from 1.22 to 2.46 with a mean value of 1.80 (Table 1). Negative Ce anomalies in BIF are commonly used as evidence for strongly oxygenated oceanic conditions during BIF deposition (Cabral et al., 2016). As a geochemical proxy for the oxidation state of sea water, it is necessary to identify the truly negative Ce anomalies in BIF by calculating La and Pr excesses. This approach is sourced from Bau and Dulski (1996), the results are shown in Fig. 5, which included all reported data of Tieshanmiao-type BIF. Although most samples displayed no negative Ce anomalies, there are four samples showed considerable negative Ce anomalies (Fig. 5). In this study, two samples (14WG-24 and 14WG-26) definitely showed true negative Ce anomalies, of which $Ce/Ce^*_{(SN)}$ are 0.89 and 0.85, respectively (Table 1).

Some characteristic ratios such as Y/Ho, Eu/Sm and Sm/Yb have also shown in Fig. 6, both P-BIF and Q-BIF in this area have no systematic differences. Most samples locate within a three-member triangle, including high-T fluid, North Pacific Deep Water (NPDW) and Upper Continental Crust (UCC) (Fig. 6).

5.2. Zircon U-Pb ages and trace elements

Zircon grains recovered from one ore sample (14WG-3) and two associated paragneisses (14WG-36 and 14WG-37) have been dated in-situ by LA-ICPMS, and the results are listed in Table 2. They are elongate to short prismatic, ranging in length from 50 μm to 200 μm with aspect ratios of 1.5:1 to 2.5:1, and displaying fragmented or slightly rounded crystal forms (Fig. 7). Cathodoluminescence images reveal that most detrital zircon crystals generally have oscillatory zoning (Fig. 7b, d and f), and high Th/U ratios (most > 0.4) (Table 2). Because oscillatory zonings and low to variable luminescence are characteristics of magmatic zircons (Hanchar and Rundnick, 1995), we interpret that these detrital zircons were igneous in origin. However, it is worth to note that there always presents less metamorphic zircon crystals with low Th/U ratios (< 0.4), and show in italics in Table 2. In this study, we chose the data with > 90% concordance, Th/U ratios > 0.4, and zircons with well-preserved oscillatory zoning, as detrital zircons of magmatic origin. By contrast, the data for detrital zircons of metamorphic origin are selected by > 90% concordance, Th/U ratios < 0.1 and no oscillatory zoning. In combination with literature data (Lan

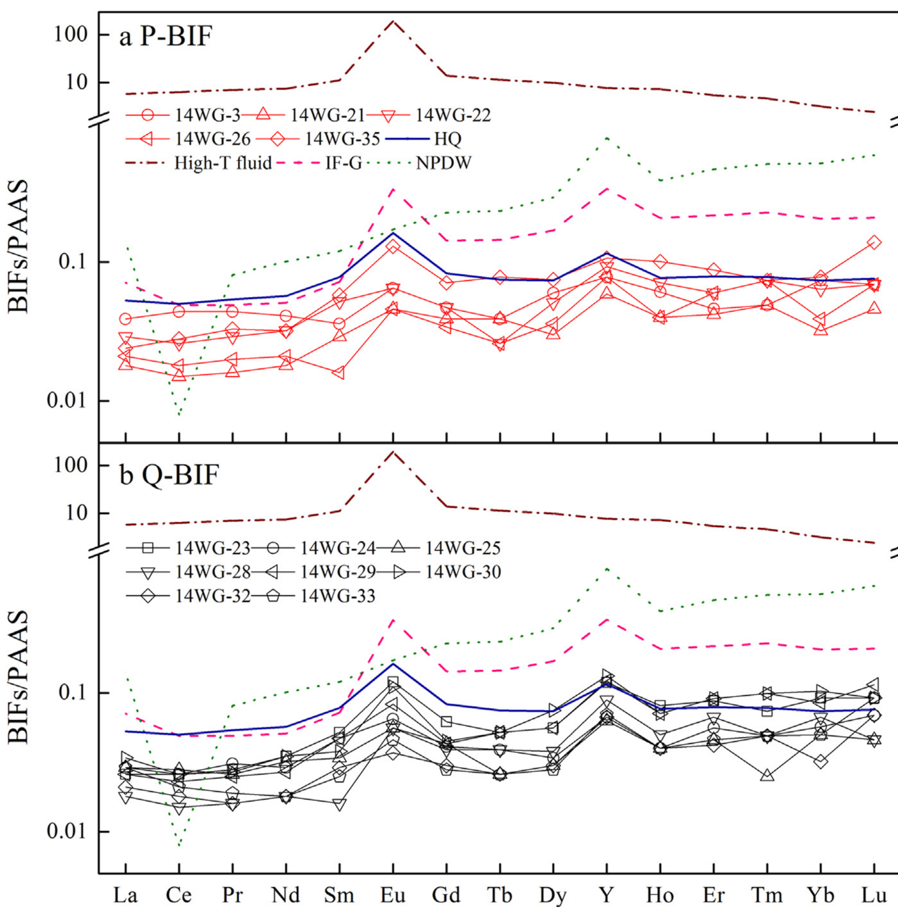

Fig. 3. PAAS-normalized REY pattern of BIF samples. (a) Iron ore samples for P-BIF; and (b) Iron ore samples for Q-BIF (PAAS values after McLennan (1989)). The nearby Huoqiu BIF (HQ) (data from Liu and Yang (2015)), high-T fluid (Bau and Dulski, 1999), Isua BIF standard IF-G (Bolhar et al., 2004), and North Pacific deep water (NPDW, Alibo and Nozaki, 1999) have also been shown.

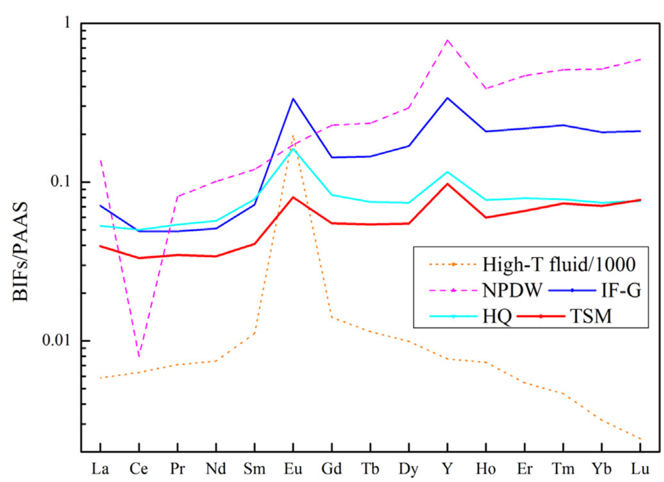

Fig. 4. PAAS-normalized REY pattern of average BIF compositions from Tieshanmiao (TSM) and Huoqiu (HQ). In addition to TSM data from this study, the other data are from Yao et al. (2015), Liu et al. (2014, 2013) and Lan et al. (2013).

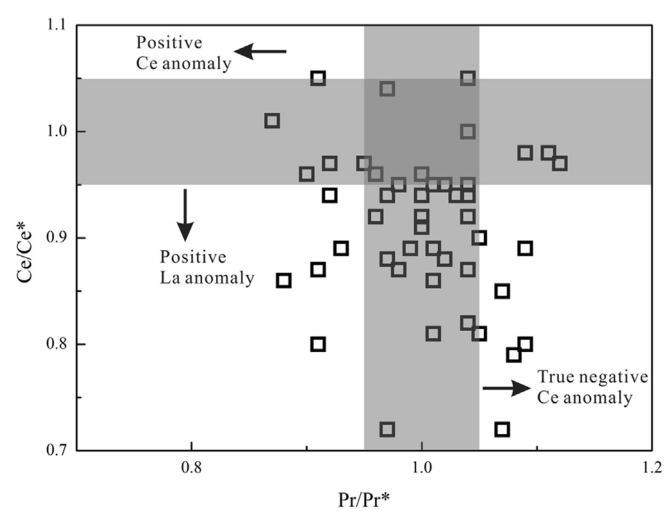

Fig. 5. Diagram of Ce/Ce* vs. Pr/Pr* used to identify La and Ce anomalies in seawater-derived sediments. The anomalies were calculated using the approach of Bau and Dulski (1996). In addition to data from this study, the other data are from Yao et al. (2015), Liu et al., (2014), Li et al., (2013) and Lan et al. (2013).

et al., 2017b; Lu et al., 2017), we drawn the age population diagrams (Fig. 8). The main age peaks are dated during 2.92–2.80 Ga (Fig. 8a), which agree well with the protolith ages of basement TTG gneisses in Wugang-Lushan complex within TH (Liu et al., 2009; Huang et al., 2010; Diwu et al., 2010; Zhou et al., 2014; Jia et al., 2016). The minimum age peak was constrained at 2.60 Ga in detrital zircons of magmatic origin from the TSM (Fig. 8a). Thirty-six detrital zircons of metamorphic origin gave two age peaks of 2.45 Ga and 1.92 Ga (Fig. 8b), respectively. The 1.92 Ga main age peak indicates an intensive metamorphism, which has been identified by previous reports (Lu et al., 2014, 2017). The maximum metamorphic age peak was constrained at 2.45 Ga (Fig. 8b), may record a regional metamorphism. Detrital zircons of magmatic origin from ZAZ also have drawn for constraining the maximum depositional ages of TSM as a result of strata succession (Figs. 8c and 1c). They gave a minimum age peak of 2.52 Ga (Fig. 8c).

Seventy zircon spots from three dated samples were analyzed by LA-

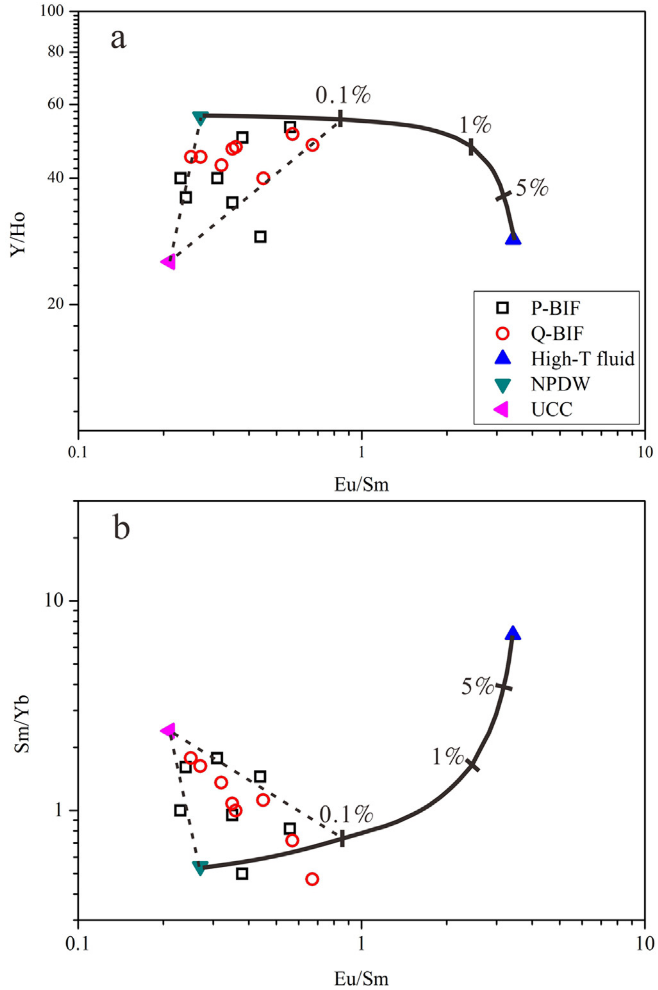

Fig. 6. Elemental ratio plots for the Wugang BIF, with two-component conservative mixing curve have also been shown. (a) Y/Ho vs. Eu/Sm, showing that a 0.1% high-T fluid contributions to BIF source is sufficient to explain Eu/Sm ratios in the Wugang BIF; (b) Sm/Yb as a function of Eu/Sm, demonstrating that 0.1% contributions of high-T fluid can model Sm/Yb and Eu/Sm behavior in the Wugang BIF. The data of high-T fluid, NPDW and upper continental crust (UCC) refer to Bau and Dulski (1999), Alibo and Nozaki (1999) and Rudnick and Gao (2003), respectively.

ICPMS for their trace elements, and the results are listed in Table 3. The chondrite-normalized REE pattern of zircons is shown in Fig. 9, which illustrates strong enrichment in HREE, significant positive Ce anomalies, and considerable negative Eu anomalies. Sample 14WG-36 has very limited variation in REE composition due to lack of metamorphic zircon. The REE patterns are similar to magmatic zircons. Ti-in-zircon temperatures were calculated by the thermometry of Watson et al. (2006), yielded zircon crystallization temperatures of 681–950 °C (Ave. 780 °C). Five spots with higher Ti contents > 200 ppm have been ignored due to mineral inclusions influence. This is also evidenced by Ti-Nb positive correlated relationship in sample 14WG-37. The common Ti-bearing minerals, such as rutile, sphene and ilmenite, are enriched in HFSE, especially Nb (Frost et al., 2001; Zack et al., 2002; Klemme et al., 2006). Thus Ti-Nb positive correlations imply Ti-bearing mineral inclusions have been ablated during trace elements analyses. Their trace compositions should been ignored, in particular, the Ti contents. Based on this, the thermometry yielded zircon crystallization temperatures of 713–951 °C (Ave. 802 °C) for sample 14WG-37, which is virtually indistinguishable from sample 14WG-36. Although only have six available data from sample 14WG-3, the calculated temperatures range from 706 °C to 936 °C with an average of 814 °C, which are indistinguishable from temperatures of two paragneisses.

5.3. Zircon Lu-Hf isotopes

In-situ Lu-Hf isotope analyses were carried out on 51 zircon grains from three dated samples, and the results are listed in Table 4. Their $\varepsilon_{Hf}(t)$ evolved diagrams are shown in Fig. 10. Most Lu-Hf analyses were performed on the same or nearby spots used for dating. The $^{207}Pb/^{206}Pb$ ages were applied in initial $\varepsilon_{Hf}(t)$ calculation and "crustal" model ages (T_{DM2}). T_{DM2} Values were calculated using a $^{176}Lu/^{177}Hf$ ratio (0.015) of average continental crust that originally was derived from the depleted mantle (Griffin et al., 2002).

Twenty-eight zircon grains from sample 14WG-36 have been analyzed, most spots displayed positive $\varepsilon_{Hf}(t)$ values, ranging from 0.3 to 12.0 (Ave. 4.1). Two spots yielded negative $\varepsilon_{Hf}(t)$ values of −2.2 and −2.4 (Table 4). The highest $\varepsilon_{Hf}(t)$ value of 12.0 with anomalous T_{DM1} and T_{DM2}, both younger than their crystallization age (spot 27). The spot 24 also displayed the similar feature (model ages younger than the crystallization ages), suggesting that their Hf isotopic compositions are insignificance. In the case of precluding the two spots data, the remaining spots gave a limited initial $^{176}Hf/^{177}Hf$ ratios varied from 0.281042 to 0.281180, corresponding $\varepsilon_{Hf}(t)$ values from −2.4 to 7.3. The single-stage Hf model ages (T_{DM1}) range from 2815 to 3004 Ma and the "crustal" model ages range from 2807 to 3189 Ma.

Twenty zircons from sample 14WG-37 have been carried out Lu-Hf isotope analysis, the result shown they yielded a constant initial $^{176}Hf/^{177}Hf$ ratios ranging from 0.280924 to 0.281226, except for spots 1 and 13, they have anomalous model ages younger than the crystallization ages. Most spots have positive $\varepsilon_{Hf}(t)$ values from 0.5 to 7.0. Only spot 15 has the negative $\varepsilon_{Hf}(t)$ value of −1.7. The corresponding T_{DM1} and T_{DM2} are 2758–3162 Ma and 2802–3360 Ma, respectively. Five zircons from ore sample 14WG-3 gave a constant initial $^{176}Hf/^{177}Hf$ ratios ranging from 0.281020 to 0.281193, corresponding $\varepsilon_{Hf}(t)$ values of −1.5 to 4.7. T_{DM1} and T_{DM2} are 2800–3030 Ma and 2863–3220 Ma, respectively (Table 4).

6. Discussion

6.1. Ages and types of the Wugang BIF

The outcrops of Archean Taihua complex exposed in the Wugang area are far less than that nearby Lushan area, resulting in the intensive investigations on the TH rocks from Lushan area (Wan et al., 2006; Liu et al., 2009; Xu et al., 2009; Diwu et al., 2010; Lu et al., 2013; Zhou et al., 2014, 2015), but less investigations from Wugang TH rocks (Lu et al., 2014, 2017; Liu and Yang, in press), in particular, the depositional ages of the Wugang BIF (Lan et al., 2017b). Actually, based on the Wugang BIF hosted in strata of TSM, thus the depositional ages of the Wugang BIF can be constrained by the ages of TSM.

Due to lack of volcanic materials from orebody and hanging wall and footwall, we chose ore sample directly and the associated metasedimentary rocks for zircon selection. In term of detrital zircon distribution, we chose paragneiss for zircon selection due to less or no detrital zircons distributed in carbonatites and clastic rocks (major host rocks of BIF orebody). Coupled with literature data (Lan et al., 2017b; Lu et al., 2017), 110 available detrital zircon (magmatic origin) data from TSM gave a main age peak of 2.92–2.80 Ga (Fig. 8a), implying muti-episodes intensive magmatic events at Mesoarchean (Liu and Yang, in press). Kröner et al. (1988) reported 2.84 Ga zircon evaporation ages for tonalite in the Lushan area, furthermore, Liu et al. (2009) found abundant 2.84 Ga magmatic zircons in amphibolite from Lushan area by SHRIMP dating. Two observations seem pertinent. These data not only confirm the Mesoarchean age of tonalite and amphibolite at Lushan, but also that there was an episode of crustal accretion by magmatic event. Recently, this episode Mesoarchean magmatic event has been identified from many areas within TH (Jia et al., 2016; Xie

Table 2
Zircon LA-ICPMS U-Pb data for two paragneisses (PG) and one BIF sample from Tieshanmiao Formation.

Sample	Concentrations (ppm)				Isotopic ratios						Isotopic ages (Ma)						Concordance
Spot	Pb	Th	U	Th/U	$^{206}Pb/^{238}U$	1σ	$^{207}Pb/^{235}U$	1σ	$^{207}Pb/^{206}Pb$	1σ	$^{206}Pb/^{238}U$	1σ	$^{207}Pb/^{235}U$	1σ	$^{207}Pb/^{206}Pb$	1σ	(%)
14WG-36 (PG)																	
1	465	320	574	0.56	0.5418	0.0073	15.9745	0.4379	0.2099	0.0058	2791	30.7	2875	26.3	2905	44.0	97%
2	136	69	226	0.30	0.4475	0.0071	11.5378	0.3448	0.1838	0.0055	2384	31.8	2568	28.0	2688	48.9	92%
3	187	107	270	0.40	0.5008	0.0076	13.0782	0.4001	0.1852	0.0060	2617	32.8	2685	28.9	2700	53.9	97%
4	393	205	607	0.34	0.4584	0.0081	12.3398	0.4322	0.1892	0.0069	2433	36.0	2631	32.9	2735	60.2	92%
5	131	104	176	0.59	0.4974	0.0117	13.3452	0.6594	0.1884	0.0090	2603	50.6	2704	46.7	2729	79.0	96%
6	141	95	179	0.53	0.5503	0.0102	15.6593	0.5163	0.2031	0.0071	2826	42.5	2856	31.5	2852	57.9	98%
7	299	267	384	0.70	0.5303	0.0096	14.7382	0.4740	0.1973	0.0062	2743	40.4	2798	30.6	2806	51.5	97%
8	156	102	205	0.50	0.5294	0.0091	14.6383	0.5257	0.1968	0.0071	2739	38.2	2792	34.2	2800	58.6	98%
9	208	112	299	0.38	0.4934	0.0079	13.8621	0.4710	0.2003	0.0069	2585	34.1	2740	32.2	2829	56.2	94%
10	128	78	149	0.53	0.5861	0.0102	17.1088	0.5781	0.2093	0.0072	2973	41.4	2941	32.5	2900	56.2	98%
11	136	82	187	0.44	0.5203	0.0094	13.9514	0.4965	0.1923	0.0071	2701	39.7	2746	33.8	2762	60.8	98%
12	138	99	185	0.54	0.4820	0.0085	13.4868	0.5308	0.1998	0.0082	2536	37.0	2714	37.2	2825	66.7	93%
13	144	111	221	0.50	0.4546	0.0082	10.8492	0.4186	0.1709	0.0069	2416	36.2	2510	35.9	2569	67.6	96%
14	124	74	150	0.49	0.5607	0.0100	15.8712	0.5904	0.2021	0.0078	2870	41.5	2869	35.6	2844	63.0	99%
15	319	264	396	0.67	0.5548	0.0091	15.4066	0.5085	0.1979	0.0066	2845	37.6	2841	31.5	2809	54.9	99%
16	272	174	430	0.41	0.4704	0.0074	11.2124	0.4135	0.1693	0.0064	2485	32.5	2541	34.4	2551	62.8	97%
17	354	241	451	0.53	0.5646	0.0089	15.1933	0.5018	0.1921	0.0064	2886	36.5	2827	31.5	2761	53.9	97%
18	192	89	289	0.31	0.5003	0.0098	12.9528	0.4784	0.1844	0.0064	2615	42.2	2676	34.9	2692	57.4	97%
19	271	209	343	0.61	0.5328	0.0092	13.7024	0.4911	0.1842	0.0065	2753	38.6	2729	34.0	2691	59.1	99%
20	215	126	317	0.40	0.4748	0.0077	12.5429	0.7076	0.1885	0.0098	2505	33.6	2646	53.1	2729	86.1	94%
21	134	92	172	0.53	0.5377	0.0099	14.7480	0.6203	0.1975	0.0085	2774	41.6	2799	40.0	2806	65.7	99%
22	167	87	269	0.32	0.4762	0.0084	12.2266	0.4221	0.1835	0.0063	2511	36.6	2622	32.5	2685	56.5	95%
23	211	152	272	0.56	0.5267	0.0091	14.9209	0.4839	0.2042	0.0072	2728	38.3	2810	30.9	2860	57.4	97%
24	440	548	661	0.83	0.4219	0.0111	11.6846	0.4937	0.1952	0.0073	2269	50.4	2579	39.6	2787	61.1	87%
25	448	340	597	0.57	0.4906	0.0071	14.1045	0.4394	0.2045	0.0068	2573	30.6	2757	29.6	2862	54.8	93%
26	155	89	223	0.40	0.4878	0.0081	13.0410	0.4207	0.1912	0.0064	2561	35.2	2683	30.5	2754	53.9	95%
27	138	82	181	0.45	0.5129	0.0090	14.6183	0.4960	0.2043	0.0072	2669	38.5	2791	32.3	2861	57.1	95%
28	*235*	*93*	*331*	*0.28*	*0.5271*	*0.0147*	*12.7898*	*0.4734*	*0.1760*	*0.0070*	*2729*	*62.2*	*2664*	*34.9*	*2617*	*66.7*	*97%*
29	349	227	444	0.51	0.5426	0.0086	15.2681	0.5287	0.2012	0.0072	2794	36.0	2832	33.1	2835	59.1	98%
30	118	81	147	0.56	0.5354	0.0092	15.5191	0.5312	0.2088	0.0075	2764	38.5	2848	32.7	2898	58.3	97%
31	256	182	359	0.51	0.4637	0.0084	13.2748	0.4673	0.2039	0.0069	2456	37.0	2699	33.3	2858	60.3	90%
32	186	137	234	0.59	0.5237	0.0090	14.0770	0.5162	0.1930	0.0075	2715	37.9	2755	34.8	2768	64.7	98%
14WG-37 (PG)																	
1	315	220	406	0.54	0.5242	0.0089	15.3839	0.5221	0.2096	0.0072	2717	37.8	2839	32.4	2902	55.9	95%
2	301	597	878	0.68	0.2374	0.0069	6.0640	0.2424	0.1829	0.0060	1373	35.7	1985	34.9	2680	54.3	63%
3	449	566	787	0.72	0.3517	0.0058	9.1298	0.3219	0.1844	0.0064	1943	27.5	2351	32.3	2694	57.1	80%
4	150	92	205	0.45	0.5138	0.0095	14.6307	0.6084	0.2025	0.0084	2673	40.4	2792	39.6	2846	67.6	95%
5	559	829	876	0.95	0.3711	0.0054	9.1216	0.3347	0.1750	0.0067	2035	25.4	2350	33.6	2606	64.2	85%
6	218	201	250	0.80	0.5523	0.0097	15.6455	0.5512	0.2020	0.0072	2835	40.3	2855	33.7	2843	58.0	99%
7	229	187	288	0.65	0.5288	0.0091	14.4347	0.4686	0.1948	0.0065	2736	38.5	2779	30.9	2783	54.9	98%
8	333	376	560	0.67	0.4098	0.0071	10.1079	0.3459	0.1748	0.0061	2214	32.4	2445	31.7	2606	58.0	90%
9	102	77	139	0.56	0.5053	0.0099	14.0629	0.4933	0.1995	0.0072	2636	42.5	2754	33.3	2822	58.9	95%
10	149	113	189	0.60	0.5232	0.0085	15.1395	0.4593	0.2067	0.0065	2713	36.0	2824	29.0	2880	51.2	95%
11	175	136	219	0.62	0.5312	0.0083	15.1132	0.4558	0.2040	0.0067	2747	34.8	2822	28.8	2858	52.6	97%
12	271	280	370	0.76	0.4683	0.0073	13.3768	0.4414	0.2041	0.0073	2476	31.9	2707	31.2	2859	24.5	91%
13	250	174	289	0.60	0.5583	0.0089	17.6510	0.5629	0.2257	0.0079	2860	36.7	2971	30.7	3021	55.9	96%
14	209	135	347	0.39	0.4122	0.0079	11.5582	0.3593	0.1998	0.0067	2225	36.0	2569	29.1	2825	55.1	85%
15	215	130	296	0.44	0.5042	0.0105	14.3386	0.5048	0.2005	0.0073	2632	45.0	2772	33.5	2831	59.3	94%
16	459	357	584	0.61	0.5275	0.0092	14.6294	0.5223	0.1940	0.0078	2731	38.9	2791	34.0	2776	65.7	97%
17	*191*	*75*	*457*	*0.16*	*0.3141*	*0.0058*	*7.8792*	*0.2745*	*0.1763*	*0.0068*	*1761*	*28.5*	*2217*	*31.4*	*2620*	*64.8*	*77%*
18	151	99	211	0.47	0.4855	0.0102	14.2719	0.5597	0.2082	0.0091	2551	44.1	2768	37.3	2892	71.3	91%

(*continued on next page*)

Table 2 (*continued*)

Sample	Concentrations (ppm)				Isotopic ratios						Isotopic ages (Ma)						Concordance
Spot	Pb	Th	U	Th/U	$^{206}Pb/^{238}U$	1σ	$^{207}Pb/^{235}U$	1σ	$^{207}Pb/^{206}Pb$	1σ	$^{206}Pb/^{238}U$	1σ	$^{207}Pb/^{235}U$	1σ	$^{207}Pb/^{206}Pb$	1σ	(%)
19	137	82	179	0.46	0.5462	0.0124	15.3832	0.6413	0.1985	0.0082	2809	51.9	2839	39.8	2815	66.8	98%
20	270	104	440	0.24	0.4664	0.0083	13.5154	0.5216	0.2038	0.0081	2468	36.7	2716	36.5	2856	64.5	90%
21	405	305	521	0.59	0.5244	0.0084	14.8333	0.5282	0.1991	0.0073	2718	35.7	2805	33.9	2820	61.3	96%
22	333	194	577	0.34	0.4247	0.0079	10.9475	0.3862	0.1815	0.0064	2282	35.9	2519	32.9	2733	58.3	90%
23	275	140	387	0.36	0.5307	0.0098	14.2439	0.5067	0.1885	0.0066	2744	41.2	2766	33.8	2729	58.5	99%
24	452	424	642	0.66	0.4656	0.0099	12.6406	0.5075	0.1886	0.0072	2464	43.6	2653	37.8	2729	62.7	92%
25	176	115	252	0.45	0.5020	0.0080	14.6620	0.4890	0.2070	0.0073	2623	34.4	2794	31.8	2883	57.4	93%
26	299	277	354	0.78	0.5431	0.0081	15.8203	0.5190	0.2069	0.0073	2796	33.8	2866	31.4	2883	57.4	97%
27	134	84	181	0.46	0.5276	0.0138	16.0011	0.7048	0.2165	0.0096	2731	58.2	2877	42.1	2955	70.5	94%
28	311	372	365	1.02	0.4973	0.0106	15.4661	0.6870	0.2197	0.0096	2602	45.6	2844	42.4	2989	70.7	91%
29	389	416	466	0.89	0.5022	0.0092	15.6226	0.6347	0.2200	0.0091	2623	39.3	2854	38.8	2981	66.7	91%
30	156	119	210	0.57	0.5209	0.0140	15.8343	0.6851	0.2160	0.0089	2703	59.5	2867	41.4	2951	66.7	94%
31	*139*	*19*	*280*	*0.07*	*0.4178*	*0.0085*	*11.4591*	*0.4060*	*0.1942*	*0.0073*	*2250*	*38.7*	*2561*	*33.1*	*2777*	*61.1*	*87%*
32	345	371	462	0.80	0.4681	0.0096	13.5416	0.4688	0.2034	0.0076	2475	42.0	2718	32.8	2853	60.5	90%
14WG-3 (BIF)																	
1	*603*	*113*	*1369*	*0.08*	*0.4027*	*0.0094*	*10.3005*	*0.3938*	*0.1809*	*0.0060*	*2182*	*43.2*	*2462*	*35.4*	*2661*	*55.4*	*87%*
2	*682*	*212*	*1494*	*0.14*	*0.3694*	*0.0057*	*9.6369*	*0.2824*	*0.1848*	*0.0053*	*2026*	*26.7*	*2401*	*27.0*	*2696*	*46.5*	*83%*
3	547	347	757	0.46	0.5181	0.0069	14.1137	0.3687	0.1942	0.0055	2691	29.1	2757	24.8	2789	46.0	97%
4	702	967	1506	0.64	0.3136	0.0074	7.9746	0.2242	0.1821	0.0052	1758	36.5	2228	25.4	2672	48.3	76%
5	665	404	1105	0.37	0.4379	0.0061	11.3448	0.2879	0.1839	0.0047	2341	27.6	2552	23.7	2689	37.5	91%
6	2490	1394	4172	0.33	0.4596	0.0075	12.4583	0.3429	0.1917	0.0048	2438	33.3	2640	25.9	2757	40.3	92%
7	220	311	1439	0.22	0.1137	0.0034	2.3927	0.1273	0.1493	0.0070	694	19.6	1240	38.1	2339	81	43%

Notes: Italics denote the metamorphic zircons based on their Th/U ratios and CL images.

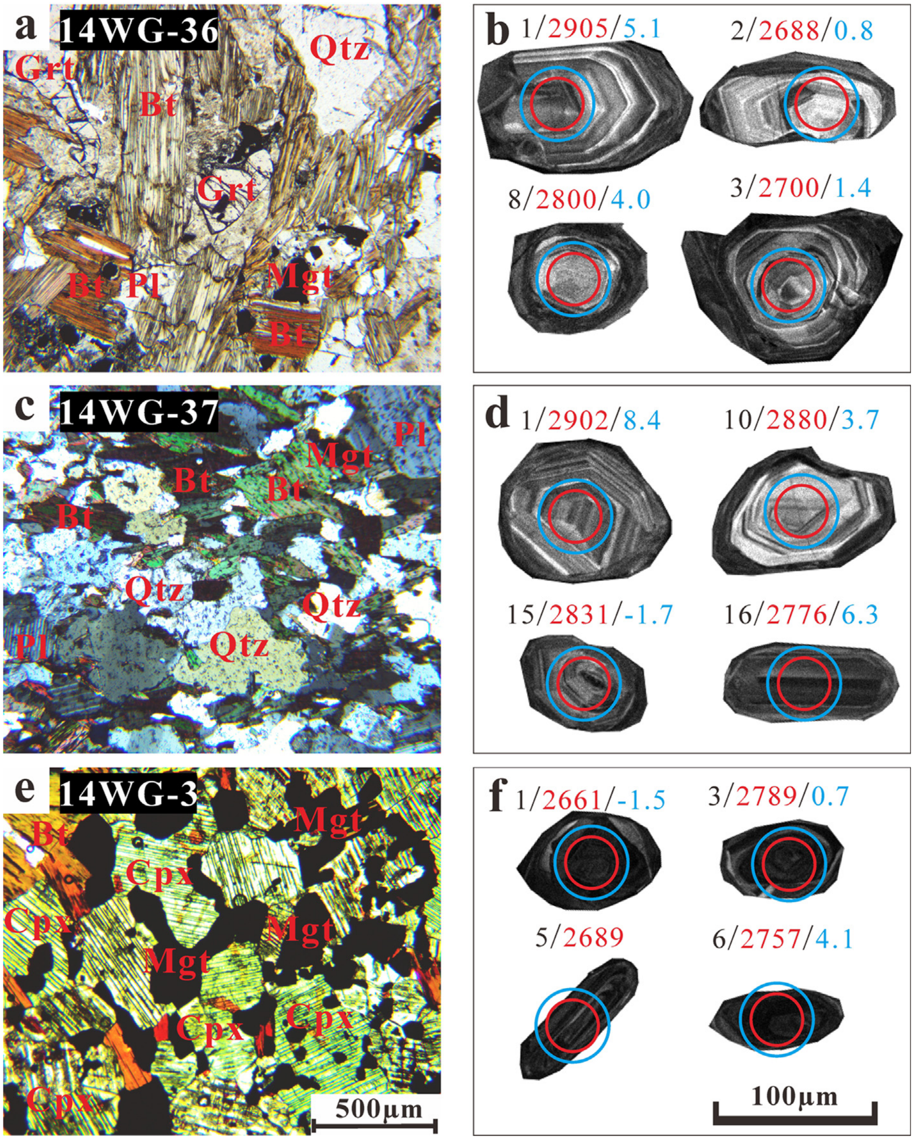

Fig. 7. Left panels show photomicrographs and right panels show their corresponding zircon CL images for two garnet gneisses (14WG-36 and 14WG-37) and a BIF sample (14WG-3). (a, b) photomicrograph under plane polarized light and zircon CL image for sample 14WG-36; (c, d) photomicrograph under crossed polar and zircon CL image for sample 14WG-37; (e, f) photomicrograph under plane polarized light and zircon CL image for sample 14WG-3. The red and blue circles denote the ablated locations for U-Pb and Lu-Hf analyses, respectively. The black, red and blue number close to the circle are the analysis spot number, $^{207}Pb/^{206}Pb$ age and corresponding $\varepsilon_{Hf}(t)$ value, respectively. (For interpretation of the references to colour in this figure legend, the reader is referred to the web version of this article.)

et al., 2016; Zhou et al., 2014), which further demonstrated the existence of Mesoarchean basement on a certain scale. However, 2.76 Ga tonalite, TTG-like gneisses and Yushuzhuang gneisses (geochemical features similar to TTG, Yang et al., 2008) from Lushan block have been reported in previous references (Xue et al., 1995; Diwu et al., 2010; Huang et al., 2010; Xie et al., 2016), and the coeval leucocratic gneisses have also been found from the Huoqiu complex at the southeastern margin of NCC (Liu et al., 2015, 2016; Wang et al., 2014). These TTG or TTG-like rocks have demonstrated a key magmatic event at 2.76 Ga, where is widespread in NCC for juvenile crust growth (Zhai and Santosh, 2013; Zhao and Zhai, 2013), constituting the widespread basement in this unit. This age interval has also been recorded in detrital zircons, which is shown as the second age peak (Fig. 8a). Moreover, most $\varepsilon_{Hf}(t)$ values of detrital zircons in this study displayed positive values (Fig. 10), consistent with magmatic zircons from TTG gneisses and amphibolites (Liu et al., 2009; Liu and Yang, in press; Huang et al., 2010; Diwu et al., 2010; Zhou et al., 2014; Jia et al., 2016). On the basis of discussions above-mentioned, it is reasonable to suggest these detrital zircons are proximal. Their minimum ages are commonly regard as the maximum depositional ages, but in this study only two detrital zircons record the minimum ages of 2.56 Ga. In this case, the minimum age peak is more robust evidence for the maximum depositional age. Therefore, we chose the minimum age peak at 2.60 Ga as the maximum depositional age of TSM, also indicating an upper limit age for Wugang BIF.

Thirty-six metamorphic zircons from TSM gave the available metamorphic age distribution diagram (Fig. 8b). Two metamorphic ages of 2.45 Ga and 1.92 Ga have been documented. High resolution SIMS U-Pb dating of the metamorphic zircons has demonstrated that Wugang block suffered peak metamorphism at 1.92 Ga (Lu et al., 2014; 2017). Zircons from two amphibolites (L65 and L66) in the TSM gave a constant age of 2.45 Ga, which is interpreted to possibly represent the formation age of the protolith of the amphibolites (Lu et al., 2014). However, the dark domain and no oscillatory zoning in CL images (Fig. 7b and c in their text) and low Th/U ratios (most < 0.4, Table 3 in their text) of 2.45 Ga zircons indicate this age is a metamorphic age instead of protolithic age. Actually, two zircons from the BIF sample (14WG-3) also have recorded this metamorphic age. They have low Th/U ratios (0.08 and 0.14, respectively) and dark core domain (Fig. 7f). Therefore, we suggest that 2.45 Ga can represent the lower limit age for the deposition of the Wugang BIF.

ZAZ has often been considered as the successive strata underlying the TSM, the initial depositional age of the TSM is a little later than or nearly the age of ZAZ (Lan et al., 2017b). The strongest age peak of detrital zircons is constrained at 2.52 Ga for ZAZ (Fig. 8c), but this age information has no any records in TSM (Fig. 8a). The likely

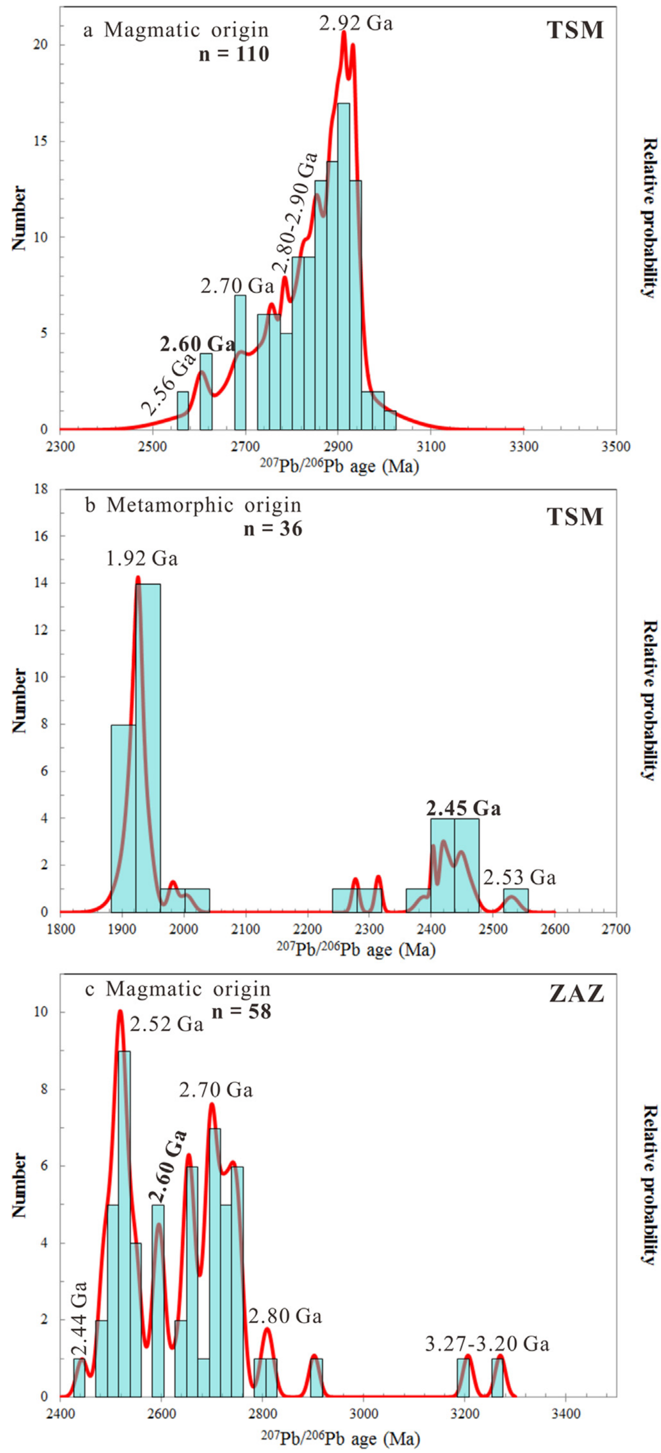

Fig. 8. U-Pb age histogram showing the results of all detrital zircon analyses from this study (14WG-36, 14WG-37 and 14WG-3) and other literature (Lan et al., 2017b; Lu et al., 2017). Data for detrital zircons of magmatic origin were filtered by > 90% concordance, Th/U ratios > 0.4 and well-documented oscillatory zoning; whereas the metamorphic origin were selected by > 90% concordance, Th/U ratios < 0.1 and no oscillatory zoning. (a) Detrital zircons of magmatic origin from TSM; (b) detrital zircons of metamorphic origin from TSM; and (c) detrital zircons of magmatic origin from ZAZ. n, number of available detrital zircon. The number above peak is defined by the probability curves as shown.

interpretation is that 2.52 Ga plutons emplace into ZAZ but do not extend to TSM. Indeed, extensive plutons have been identified from the southern margin of the NCC, such as Xutai granitic plutons (dated at 2509 ± 33 Ma; Zhou et al., 2011). Thus we propose that the minimum age peak of 2.52 Ga from ZAZ probably documents the emplacement age. It is not suitable for constraining the time of ZAZ stratum, especially of TSM.

Gross (1980) divided the Precambrian BIFs into two types, Algoma-type and Superior-type based on depositional setting, where the former generally associated with mafic volcanic rocks erupted on the seafloor, the latter were common deposited in continental margin or back-arc basin with less or no volcanic material in orebody. Huston and Logan (2004) pointed out that Algoma-type BIFs are characterized by much larger Eu anomalies (> 1.8) than Superior-type BIFs (< 1.8). This difference suggests that there is much larger component of volcanic-related hydrothermal emanations in Algoma-type BIFs but less in Superior-type BIFs, reflecting the important differences in the depositional distance away from the submarine vent (Bekker et al., 2010; Li et al., 2012). Previous studies suggested that the Wugang BIF belong to Algoma-type, mostly according to the similarity with Anshan-Benxi iron deposit in the Northern NCC (Yu et al., 1981; Wang et al., 2006; Luo, 2009; Liu et al., 2014), but neglecting the significant differences between each other. In this study, we propose that the Wugang BIF belongs to Superior-type, and the evidence is as follows: (1) both hanging wall and footwall for most BIF orebodies are marble, quartzite and schist in this unit, moreover, a lack of volcanic materials in orebody, e.g., Tiegukeng deposits (Fig. 2); (2) most BIF samples display relatively low Eu anomalies (< 1.8, Table 1), akin to Superior-type; (3) proximal detrital zircons appear in BIF samples, suggest crustal contamination by terrestrial material or riverine input, but widespread low Al, Ti, Zr, Th, Nb and Sc in BIF samples precluding considerable terrestrial material input, therefore, the most likely approach is riverine input, which indicates a continental marginal or back-arc basin setting; (4) there are four samples displayed considerable true negative Ce anomalies (Fig. 5), indicating the depositional setting is in shallow sea environment.

The largest debate is from the origin of the P-BIF, due to abundant pyroxene distribution. Li et al. (2014) suggested that the P-BIF are products of chemical deposition affected by the volcanic eruption on the basis of magnetite composition, mineralogical and microfabric characteristics. However, geological and geochemical characteristics of P-BIF and Q-BIF indicate they possess similar material source and genetic mechanism (Yao et al., 2015). It can be excluded that pyroxene sourced from argillaceous sediment in the origin (Lan et al., 2013), but most likely formed from reaction between ankerite or siderite and quartz, these metamorphic mechanisms have also been described in detailed in Yao et al. (2015). Actually, P-BIF have very similar chemical compositions with Q-BIF in this study (Fig. 3). This demonstrate that P-BIF are high-grade metamorphic products of Q-BIF and carbonate. Therefore, both sub-types of P-BIF and Q-BIF in Wugang unit belong to Superior-type BIF.

6.2. Source characteristics

Studies on Fe source of BIF can be divided into three stages: (1) early studies suggested a continental source of Fe for BIF (e.g., Cloud, 1973; Lepp and Goldich, 1964); (2) the similarity between hydrothermal fluid (e.g., positive Eu anomalies) and BIFs, and similar REY characteristics (e.g., positive Y anomalies) between seawater and BIFs, led to a commonly accepted model, in which BIF source from mixture of hydrothermal fluid and seawater (e.g., Derry and Jacobsen, 1990; Bau and Möller, 1993; Bau and Dulski, 1996; Bolhar et al., 2004; Huston and Logan, 2004); (3) Recent work, particularly the combination of Nd and Fe isotopes and REY, suggest a significant component sourced from the continents by riverine input (e.g., Alexander et al., 2008, 2009; Haugaard et al., 2013; Li et al., 2015).

BIFs have generally very low concentrations of incompatible elements such as Al, Ti, Zr, Th, Nb and Sc, indicating an authigenic origin. The fractionation of rare earth elements (REE) during BIF formation is

Table 3
Trace element compositions of zircons (in ppm) from paragneisses (PG) and BIF from Tieshanmiao Formation.

LA/spot	Ti	Y	Nb	Ta	La	Ce	Pr	Nd	Sm	Eu	Gd	Tb	Dy	Y	Ho	Er	Tm	Yb	Lu	Y/Ho	$(Yb/Sm)_N$ [a]	$(Lu/Gd)_N$ [a]	Eu/Eu* [b]	Ce/Ce* [c]	T (°C) [d]
14WG-36 (PG)																									
1	27.7	2826	4.17	1.58	3.14	45.0	1.70	12.6	12.2	4.63	52.4	18.6	218	2826	85.8	406	87.9	910	180	33	67.1	27.8	0.6	4.8	839
2	14.4	2418	2.83	1.17	0.30	21.7	0.51	6.54	8.01	3.51	45.7	15.1	193	2418	75.7	365	79.3	837	163	32	94.0	28.8	0.6	13.6	774
3	20.6	1519	3.14	1.20	0.65	22.2	1.25	11.0	9.78	5.24	32.8	9.56	113	1519	44.9	229	51.6	546	113	34	50.3	27.8	0.9	6.0	809
4	9.18	2340	1.99	1.26	1.33	32.3	1.95	15.6	15.3	10.00	54.7	16.7	195	2340	73.1	334	71.1	768	152	32	45.1	22.5	1.1	4.9	733
5	4.83	3311	2.24	0.79	0.89	32.9	1.74	22.7	18.3	20.0	86.0	23.2	281	3311	109	485	96.7	966	180	30	47.4	16.9	1.5	6.5	681
6	29.7	3019	3.22	1.10	0.84	27.4	1.08	8.78	11.1	9.10	60.7	20.3	249	3019	96.6	450	92.6	964	182	31	78.0	24.3	1.1	7.1	847
7	71.9	5096	4.03	1.41	28.2	117	10.4	55.7	32.4	5.72	123	37.4	431	5096	163	749	154	1570	287	31	43.6	18.9	0.3	1.7	950
8	44.8	2875	3.02	1.58	1.24	32.2	1.13	11.4	13.3	4.98	64.2	19.1	252	2875	93.6	425	86.8	907	169	31	61.3	21.3	0.5	6.7	893
9	11.5	2899	4.85	1.87	0.23	34.5	0.35	4.07	5.92	2.65	45.9	17.2	223	2899	91.1	436	97.4	1037	198	32	157.8	34.9	0.5	29.9	754
10	15.6	2397	3.05	1.15	0.011	23.1	0.14	3.68	6.35	1.45	42.0	15.0	186	2397	76.3	356	75.5	780	155	31	110.5	29.8	0.3	141.3	782
11	22.1	2353	3.44	1.51	1.38	29.4	0.82	6.87	7.74	1.96	42.2	14.9	183	2353	74.3	346	75.3	776	146	32	90.2	28.0	0.3	6.8	816
12	9.19	3080	2.83	1.07	0.91	32.4	1.66	19.1	17.1	5.36	66.2	22.3	256	3080	97.1	451	92.6	953	184	32	50.1	22.4	0.5	6.5	734
13	5.45	2484	2.91	1.43	0.28	26.2	0.31	4.46	7.85	1.92	48.4	17.2	208	2484	78.6	369	78.0	787	150	32	90.2	25.1	0.3	21.9	690
14	12.6	2149	2.63	1.04	0.26	21.4	0.22	3.44	6.67	1.54	34.8	13.1	168	2149	66.7	324	68.0	727	143	32	98.1	33.2	0.3	21.7	762
15	11.6	2780	2.95	1.16	7.43	58.5	4.05	24.0	18.7	15.7	61.1	19.6	226	2780	87.3	391	84.8	887	179	32	42.7	23.7	1.4	2.6	754
16	23.7	4941	3.17	1.65	1.45	41.6	1.90	18.3	22.0	11.3	104	35.6	423	4941	161	736	157	1621	300	31	66.4	23.3	0.7	6.2	823
17	13.3	1755	3.72	1.46	0.34	30.9	0.45	4.05	5.64	2.78	29.2	11.0	133	1755	50.8	252	54.9	604	120	35	96.3	33.3	0.7	19.4	767
18	17.5	2216	3.82	1.63	16.7	76.3	6.45	31.0	12.0	7.46	43.2	14.1	176	2216	68.8	331	72.0	760	148	32	57.0	27.8	1.0	1.8	793
19	8.65	4703	5.82	1.77	2.12	50.3	1.73	14.8	18.8	7.33	90.4	31.9	391	4703	152	700	144	1453	272	31	69.7	24.3	0.5	6.4	728
20	17.1	3245	3.42	1.47	0.75	35.2	0.86	9.59	13.3	8.91	66.0	21.8	256	3245	101	483	103	1059	202	32	71.7	24.7	0.9	10.8	791
21	8.90	3121	2.45	1.16	1.74	25.1	1.36	11.6	13.6	3.23	66.0	22.1	259	3121	103	456	97.6	1009	191	30	66.8	23.4	0.3	4.0	731
22	329	3015	3.79	1.43	1.86	40.4	1.96	18.1	17.7	14.1	65.7	19.9	243	3015	94.5	448	98.8	1022	196	32	52.0	24.2	1.3	5.2	1181
23	11.1	3542	4.62	1.75	0.24	38.1	0.49	7.91	13.2	3.62	69.2	23.3	299	3542	114	530	110	1133	214	31	77.0	25.0	0.4	26.9	750
24	19.8	4294	10.2	2.96	2.24	81.0	2.37	16.1	17.2	5.96	80.2	26.5	339	4294	136	637	137	1428	274	32	74.7	27.6	0.5	8.6	805
25	117	2573	4.36	1.73	2.05	54.1	2.32	18.4	14.1	9.21	52.0	15.8	200	2573	77.0	371	78.3	849	170	33	54.2	26.5	1.0	6.1	1016
26	27.3	2214	3.77	1.56	3.07	37.1	1.79	13.2	8.74	3.48	40.5	13.5	172	2214	69.1	330	72.5	769	150	32	79.2	30.0	0.6	3.9	838
27	10.3	1978	2.67	1.20	16.7	82.1	9.14	48.3	21.4	4.16	51.1	14.3	166	1978	63.3	299	60.7	657	124	31	27.6	19.6	0.4	1.6	743
28	549	2523	4.05	1.60	1.24	29.8	1.32	15.4	14.2	6.37	54.3	16.4	192	2523	77.5	386	82.0	899	174	33	56.9	25.9	0.7	5.7	1280
29	326	2039	3.50	1.60	0.79	34.1	1.04	9.04	8.79	4.52	44.9	13.9	162	2039	61.3	296	61.7	690	137	33	70.7	24.6	0.7	9.2	1179
30	10.7	2555	2.97	0.95	2.24	25.8	1.23	10.4	9.57	3.58	50.2	17.3	209	2555	82.1	383	82.1	849	160	31	79.9	25.8	0.5	3.8	747
31	212	3757	5.69	1.96	1.41	51.7	1.81	15.9	17.7	9.93	79.8	24.9	309	3757	120	568	116	1209	224	31	61.3	22.7	0.8	7.9	1106
32	7.64	3035	3.31	1.31	0.055	32.9	0.25	5.62	10.3	2.00	64.4	21.3	255	3035	98.0	448	91.6	944	175	31	82.8	22.0	0.2	69.3	718
14WG-37 (PG)																									
1	9.46	4485	13.3	3.33	0.78	61.0	0.97	10.5	17.7	3.53	86.8	30.1	372	4485	146	664	137	1410	262	31	71.5	24.4	0.3	17.2	736
3	16.7	2954	4.84	1.21	20.3	193	13.5	86.2	58.4	10.3	131	31.2	289	2954	90.1	377	77.6	814	158	33	12.5	9.7	0.4	2.9	788
4	15.8	1383	2.81	0.95	0.78	36.8	0.74	7.04	7.52	2.06	29.8	9.35	111	1383	43.4	200	42.2	463	91.7	32	55.4	24.9	0.4	11.9	783
5	38.6	5417	6.83	1.78	15.4	241	11.7	83.2	62.3	16.2	188	50.4	506	5417	169	730	145	1461	270	32	21.1	11.6	0.5	4.4	875
6	850	5616	7.45	2.04	0.61	35.1	1.37	18.4	26.5	4.40	147	46.3	522	5616	185	774	146	1356	241	30	46.0	13.2	0.2	9.4	1376
7	10.2	6920	9.93	3.31	0.34	26.7	1.08	16.9	32.7	5.46	196	60.2	667	6920	235	977	181	1657	287	29	45.6	11.8	0.2	10.8	742
8	26.1	2476	4.37	1.04	7.46	114	8.34	59.0	31.9	7.80	97.3	21.6	206	2476	69.9	302	61.8	627	126	35	17.7	10.4	0.4	3.5	833
9	61.2	2950	2.93	1.35	0.22	19.7	0.40	6.70	12.7	2.22	65.2	20.8	259	2950	96.4	431	84.3	812	153	31	57.5	19.0	0.2	16.4	930
10	8.88	1617	2.68	0.83	4.38	37.0	1.90	11.1	10.2	2.29	40.4	12.4	136	1617	50.5	229	47.3	472	93.6	32	41.8	18.8	0.3	3.1	731
11	9.65	1374	1.76	0.53	0.097	40.3	0.25	3.57	5.49	2.07	28.1	8.52	99.1	1374	40.2	200	45.3	502	107	34	82.3	30.8	0.5	63.0	738
12	27.1	2174	3.13	0.84	3.69	68.3	1.66	14.1	15.0	5.21	54.0	16.1	182	2174	67.2	298	64.1	686	140	32	41.3	21.0	0.6	6.8	837
13	13.1	2034	1.79	0.58	0.16	16.3	0.42	5.46	9.84	5.59	50.7	15.1	173	2034	62.0	290	61.0	630	132	33	57.6	21.0	0.8	15.5	765
14	2047	4333	12.4	3.15	23.6	96.8	9.36	50.7	30.8	4.07	112	35.6	397	4333	139	595	121	1150	210	31	33.6	15.3	0.2	1.6	1609
15	12.8	1759	2.45	0.75	0.38	15.2	0.35	3.39	8.55	1.72	46.8	15.7	167	1759	55.9	238	47.7	481	88.5	31	50.7	15.3	0.3	10.3	763
16	7.20	5214	3.01	1.54	0.45	23.2	1.02	15.3	25.6	4.45	122	39.1	465	5214	172	750	145	1383	251	30	48.6	16.7	0.2	8.4	713
17	72.5	3414	6.34	2.60	6.47	50.4	4.14	23.6	17.3	3.55	66.1	23.4	275	3414	108	497	110	1129	214	32	58.8	26.2	0.3	2.4	951
18	526	2507	5.04	1.10	0.33	25.5	0.95	9.14	18.1	4.84	78.4	23.3	245	2507	75.5	306	57.1	560	103	33	27.9	10.6	0.4	11.1	1272
19	17.1	2778	2.77	1.33	0.21	22.8	0.39	6.23	9.99	1.40	54.1	18.5	240	2778	90.1	399	83.3	880	158	31	79.3	23.6	0.2	19.7	790
20	126	2622	3.51	0.74	1.57	32.0	2.05	17.8	22.7	8.73	92.6	25.8	251	2622	76.9	292	50.6	466	81.5	34	18.5	7.1	0.6	4.4	1026
21	27.5	2953	3.33	1.42	0.99	53.3	1.73	16.2	15.2	6.57	71.5	21.7	243	2953	89.3	418	88.5	963	188	33	57.0	21.3	0.6	10.0	838

(continued on next page)

Table 3 (*continued*)

LA/spot	Ti	Y	Nb	Ta	La	Ce	Pr	Nd	Sm	Eu	Gd	Tb	Dy	Y	Ho	Er	Tm	Yb	Lu	Y/Ho	$(Yb/Sm)_N$[a]	$(Lu/Gd)_N$[a]	Eu/Eu*[b]	Ce/Ce*[c]	T (°C)[d]
22	9.11	2045	2.25	0.79	3.03	60.3	2.62	19.9	16.7	4.43	56.3	18.3	182	2045	61.1	269	59.2	615	126	33	33.2	18.1	0.4	5.3	733
23	25.5	3035	5.89	2.73	0.16	29.6	0.28	4.03	8.95	2.23	54.4	18.4	250	3035	94.6	454	96.6	1015	193	32	102.1	28.6	0.3	34.3	831
24	56.6	3091	4.68	1.59	10.7	142	6.31	40.5	25.6	12.2	87.5	21.9	259	3091	91.3	421	89.2	960	187	34	33.8	17.3	0.8	4.2	920
25	30.7	3634	7.71	2.38	2.94	46.5	2.70	20.8	18.3	3.16	78.8	27.4	322	3634	117	506	99.7	962	175	31	47.2	17.9	0.3	4.1	850
26	11.8	1894	2.10	0.66	0.64	69.8	0.78	7.89	11.5	4.97	44.7	13.9	156	1894	56.9	267	55.8	605	119	33	47.5	21.5	0.7	24.3	756
27	9.35	3626	4.30	1.68	0.36	20.7	0.84	14.2	17.9	4.51	89.1	29.5	340	3626	121	518	98.9	963	166	30	48.5	15.1	0.3	9.3	735
28	12.7	3210	2.68	0.77	6.18	123	5.05	43.9	34.8	12.6	113	27.9	286	3210	99.0	430	92.9	983	196	32	25.4	14.1	0.6	5.4	763
29	13.1	2369	3.02	0.70	1.65	87.8	1.31	11.6	12.2	3.99	53.2	15.6	189	2369	72.1	341	74.5	826	166	33	60.9	25.3	0.5	14.7	766
30	15.7	2527	2.11	1.26	0.19	28.5	0.33	8.38	11.2	1.77	52.9	18.6	220	2527	76.9	356	70.0	728	134	33	58.3	20.5	0.2	28.3	782
31	16.0	658	2.04	0.78	2.31	23.3	1.93	12.2	8.82	2.28	22.4	6.32	62.5	658	19.6	80.8	14.0	139	23.6	34	14.2	8.5	0.5	2.7	784
32	53.2	2219	3.38	0.97	1.33	85.0	1.89	16.0	20.0	5.52	62.0	18.6	199	2219	65.6	292	62.5	682	136	34	30.7	17.7	0.5	13.1	913
14WG-3 (BIF)																									
1	11.4	1162	4.04	4.32	0.67	13.6	0.32	2.13	1.58	0.90	13.2	5.86	73.8	1162	32.2	173	41.2	502	109	36	286.6	66.7	0.6	7.2	753
2	245	2457	10.4	12.4	5.96	114	6.44	53.5	20.0	12.5	60.6	18.3	204	2457	75.6	349	75.3	795	152	33	35.8	20.4	1.1	4.5	1130
3	6.63	2050	3.73	1.83	24.2	85.6	6.92	29.0	11.7	2.37	46.0	14.3	162	2050	62.6	288	59.0	615	116	33	47.2	20.4	0.3	1.6	706
4	31.7	3792	5.34	2.31	4.98	103	3.20	27.9	33.1	11.8	122	37.0	368	3792	114	448	83.4	808	144	33	22.0	9.6	0.6	6.3	854
5	16.2	3699	2.93	1.56	1.54	28.2	0.85	8.77	12.4	5.76	75.2	24.3	287	3699	113	525	114	1282	261	33	93.3	28.1	0.6	6.0	785
6	31.2	4487	12.0	9.86	1.95	57.6	1.24	8.83	13.6	1.76	74.3	26.8	348	4487	135	648	142	1483	273	33	98.2	29.7	0.2	9.1	852
7	64.1	4023	3.52	2.54	3.73	24.0	1.05	8.54	9.20	3.90	66.9	25.6	325	4023	125	583	125	1377	245	32	134.8	29.6	0.5	3.0	936

Notes: Italics denote the data for zircons with mineral inclusions.

[a] Subscript N means normalization to chondrite values after Sun and McDonough (1989).

[b] $Eu/Eu^* = Eu_N/SQRT(Sm \times Gd)_N$, where N denotes the normalization to chondrite values after Sun and McDonough (1989).

[c] $Ce/Ce^* = Ce_N/SQRT(La \times Pr)_N$, where N denotes the normalization to chondrite values after Sun and McDonough (1989).

[d] T was calculated by using Ti-in-zircon thermometer of Watson et al. (2006).

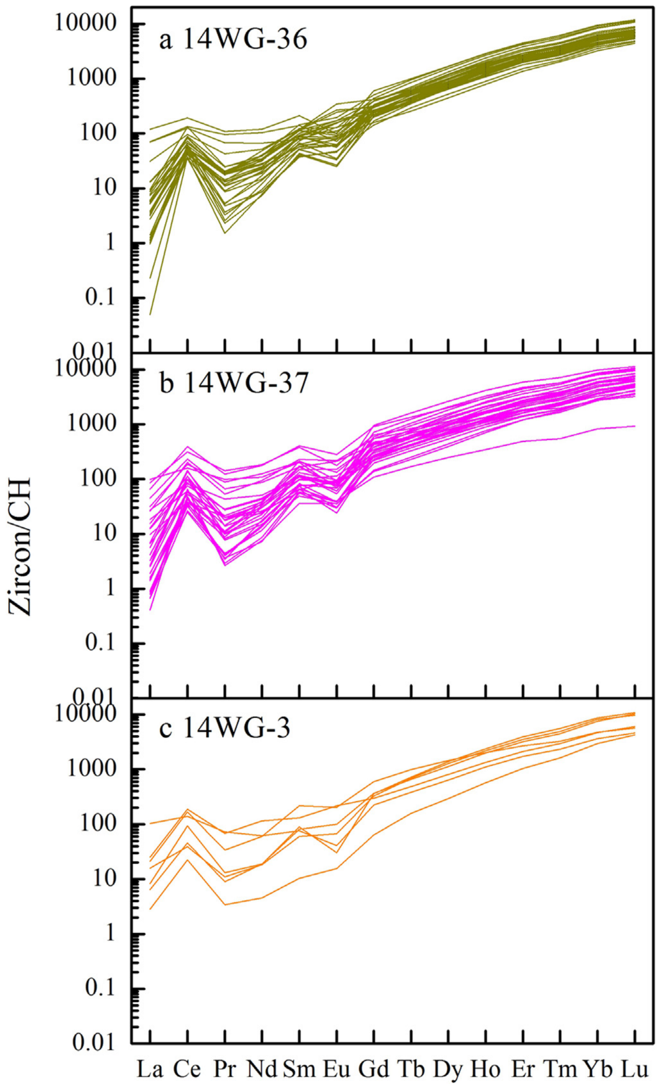

Fig. 9. Chondrite-normalized REE patterns of zircon in samples 14WG-36 (a), 14WG-37 (b) and 14WG-3 (c). Chondrite values are from Sun and McDonough (1989).

minimal (Bau and Dulski, 1996; Bolhar et al., 2004; Derry and Jacobsen, 1990; Frei and Polat, 2007; Huston and Logan, 2004; Planavsky et al., 2010). Moreover, the effect of post-depositional processes, such as diagenesis and metamorphism, on the REY distribution in BIFs is limited (Bau and Dulski, 1996; Bolhar et al., 2004). Thus, BIFs can inherit the REY signature of Fe sources at the site of mineral precipitation.

In this study, ore samples from the Wugang BIF exhibit extremely low Al_2O_3 and TiO_2 contents (< 0.67 wt%, Table 1), indicating the contribution of terrigenous clastic material can be ignored (Kato et al., 1996). Moreover, all ore samples also have extremely low concentrations of HFSE (Zr, Hf, Th and Sc), which are generally enriched in evolved continental crust. Therefore, terrigenous clastic materials are not likely to be the source during BIF chemical deposition processes. Their REY signature are shown in Figs. 3 and 4. The Y/Ho ratios of 14 whole-rock BIF samples varied from 29 to 53 with an average of 43, which are higher than the UCC and high-T hydrothermal fluid (Fig. 6a), most closely approximate those of seawater (43–80) (Nozaki et al., 1997), and suggesting considerable seawater involvement in the deposition of the Wugang BIF. All ore samples displayed positive Eu anomalies (Fig. 3), and their $Eu/Eu^*_{(SN)}$ ratios varied from 1.26 to 2.68 with an average of 1.74, a feature inherited from high-T hydrothermal fluid (Derry and Jacobsen, 1990; Bau and Dulski, 1999), suggesting that the high-T hydrothermal fluids are participated in the genesis of the Wugang BIF. The characteristic REY ratios, such as Y/Ho, Eu/Sm and Sm/Yb, plotted into a triangle field with three endmembers of high-T fluid, seawater and UCC (Fig. 6), implying that crustal contamination by terrestrial clastic material or riverine input. But constant low Al, Ti, Zr, Th, Nb and Sc in BIF samples precluding the terrestrial clastic material input, therefore, riverine input seem to supply the Fe source for BIF. Although modern rivers have very low-Fe contents (Fantle and DePaolo, 2004; Yamaguchi et al., 2005), the dissolved Fe fluxes at ~2.5 Ga could have been sufficiently large for depositing BIF (Holland, 1984), a high-Fe dissolved riverine flux would be expected prior to Neoarchean time (Li et al., 2015), providing robust evidence for riverine input as the source of BIF.

In summary, the source for the Wugang BIF contained high-T hydrothermal fluid, seawater and riverine input. Based on Fig. 6, a 0.1% high-T fluid contributions to BIF source is sufficient to explain Eu/Sm and Sm/Yb ratios in the Wugang BIF, indicating the 1000:1 mixing ratios between seawater and high-T fluid, which is in good agreement with previous studies (Khan et al., 1996; Delvigne et al., 2012; Wang et al., 2017).

6.3. *Depositional environment*

The Wugang BIF belongs to a supracrustal succession in a possible greenstone belt environment, overlying a widespread 2.76 Ga TTG-basement within TH. Although they have undergone amphibolite-granulite facies metamorphism (Lan et al., 2013, 2017b; Yao et al., 2015), some Q-BIF still retained original finely banded texture (e.g., Fig. 2b). The alternating, distinct magnetite- and silica-rich bands in Q-BIF reflect stable depositional conditions during precipitation. The prevalence of finely laminated in mirco- to meso-banded Wugang BIF sequences leads to the conclusion that they were deposited in basins deeper than at least 200 m, which is the average depth of the modern storm wave base (Trendall, 2002), due to wave action is a key factor for disturbing deposition. The absence of detrital component in the Wugang BIF, and the extremely low Al, Ti, Zr, Th, Nb and Sc in BIF samples, which also supported the deep water deposition. However, this seems to conflict with 10% BIF samples have true negative Ce anomalies in this area (Fig. 5), indicating these BIFs are deposited in oxidization conditions of surface water. A model with a stratified water column can be harmonize with each other. Ferrous iron oxidation in the marine surface water leads insoluble ferric iron further precipitate in deep water, where the lack of negative Ce anomalies for most Wugang BIF. The absence of negative Ce anomalies suggests that the water column from which most BIF precipitated was reducing with respect to Mn. The extremely low Mn contents (< 0.31 wt%) and their high Fe/Mn ratios indicate that Mn(II) was not oxidized during the precipitation of the Wugang BIF (Wang et al., 2017). Moreover, the occurrence of magnetite as the main Fe-host mineral suggest that the redox level of the seawater permitted nearly continuous precipitation of ferric oxy-hydroxides (Haugaard et al., 2013).

Most minerals in the Wugang BIF are of secondary origin, e.g., pyroxene, ankerite and siderite etc., this make it essentially impossible to deduce the original primary phases that precipitated. However, the extensive presence of the carbonate minerals at least suggests that the supersaturation of carbonate in the palaeobasin, which only could have happened above the Archean carbonate compensation depth (CCD). This depth is unknown, but due to higher P_{CO2} (the fugacity of CO_2) in the Archean atmosphere, the CCD must have been shallower in Archean time (Kramers, 2002; Haugaard et al., 2013). Moreover, close to the continental margins, the CCD tends to shoal as a result of higher biological productivity. Very low amount of detrital components, but significant UCC signatures (Fig. 6) in the Wugang BIF suggest the riverine input involved in BIF deposition, and preclude the possibility of abyssal plain deposit because of the expected rare influx of allochthonous

Table 4
Lu-Hf isotope analysis results of zircons from paragneisses (PG) and BIF from Tieshanmiao Formation.

Sample/Spot	Age (Ma)	$^{176}Lu/^{177}Hf$	$^{176}Yb/^{177}Hf$	$^{176}Hf/^{177}Hf$	1σ	$^{176}Hf/^{177}Hfi$[a]	ε_{Hf} (t)	1σ	T_{DM1} (Ma)	T_{DM2} (Ma)	$f_{Lu/Hf}$
14WG-36 (PG)											
1	2905	0.000608	0.014934	0.281100	0.000007	0.281066	5.1	0.25	2966	3004	−0.98
2	2688	0.000929	0.024025	0.281137	0.000007	0.281089	0.8	0.25	2942	3095	−0.97
3	2700	0.000641	0.015114	0.281130	0.000007	0.281097	1.4	0.25	2929	3070	−0.98
4	2735	0.001338	0.033780	0.281203	0.000007	0.281132	3.5	0.25	2883	2970	−0.96
5	2729	0.001081	0.027881	0.281103	0.000009	0.281047	0.3	0.33	2999	3160	−0.97
6	2852	0.000976	0.024818	0.281125	0.000006	0.281072	4.0	0.23	2961	3027	−0.97
7	2806	0.000869	0.022394	0.281138	0.000007	0.281092	3.7	0.26	2935	3013	−0.97
8	2800	0.001190	0.030420	0.281169	0.000009	0.281106	4.0	0.31	2917	2987	−0.96
9	2829	0.001596	0.040164	0.281266	0.000009	0.281180	7.3	0.31	2815	2807	−0.95
10	2900	0.000994	0.024876	0.281137	0.000008	0.281082	5.5	0.30	2947	2975	−0.97
11	2762	0.001039	0.025910	0.281176	0.000008	0.281121	3.7	0.27	2897	2978	−0.97
12	2825	0.001267	0.031836	0.281121	0.000009	0.281053	2.7	0.34	2989	3085	−0.96
13	2569	0.000968	0.024646	0.281128	0.000008	0.281080	−2.2	0.27	2957	3189	−0.97
14	2844	0.001125	0.029681	0.281153	0.000011	0.281091	4.5	0.40	2935	2989	−0.97
15	2809	0.000969	0.024224	0.281135	0.000008	0.281083	3.4	0.28	2947	3031	−0.97
16	2551	0.000876	0.021689	0.281130	0.000009	0.281087	−2.4	0.34	2947	3187	−0.97
17	2761	0.000662	0.015923	0.281160	0.000007	0.281125	3.8	0.26	2890	2969	−0.98
18	2692	0.000850	0.021020	0.281148	0.000008	0.281104	1.5	0.30	2921	3059	−0.97
19	2691	0.001398	0.035746	0.281214	0.000009	0.281142	2.8	0.33	2872	2977	−0.96
20	2729	0.001201	0.030108	0.281188	0.000009	0.281125	3.1	0.33	2893	2990	−0.96
21	2806	0.001449	0.035577	0.281175	0.000009	0.281097	3.9	0.33	2929	3001	−0.96
23	2860	0.001067	0.030871	0.281167	0.000017	0.281109	5.5	0.60	2911	2941	−0.97
24	2787	0.001368	0.032912	0.281323	0.000008	0.281250	8.9	0.27	2719	2680	−0.96
25	2862	0.000923	0.022225	0.281197	0.000010	0.281147	6.9	0.34	2859	2858	−0.97
26	2754	0.001087	0.027181	0.281100	0.000008	0.281042	0.7	0.29	3004	3154	−0.97
27	2861	0.001103	0.027372	0.281351	0.000007	0.281290	12.0	0.25	2663	2546	−0.97
14WG-37 (PG)											
1	2902	0.001528	0.038919	0.281246	0.000009	0.281161	8.4	0.32	2838	2801	−0.95
2	2680	0.001754	0.049883	0.281316	0.000008	0.281226	5.5	0.29	2758	2802	−0.95
3	2694	0.000753	0.018255	0.281133	0.000007	0.281094	1.2	0.25	2934	3080	−0.98
5	2606	0.001608	0.043260	0.281236	0.000008	0.281156	1.3	0.27	2858	3002	−0.95
7	2783	0.001452	0.039839	0.281244	0.000007	0.281167	5.8	0.27	2834	2864	−0.96
8	2606	0.001004	0.023618	0.281184	0.000012	0.281134	0.5	0.42	2883	3050	−0.97
9	2822	0.001060	0.027318	0.281168	0.000009	0.281111	4.7	0.31	2909	2961	−0.97
10	2880	0.000421	0.009974	0.281067	0.000009	0.281044	3.7	0.34	2997	3069	−0.99
11	2858	0.000465	0.010536	0.281093	0.000007	0.281068	4.0	0.26	2965	3031	−0.99
12	2859	0.000915	0.023149	0.281175	0.000010	0.281124	6.1	0.36	2890	2908	−0.97
13	3021	0.000861	0.020415	0.281096	0.000009	0.281046	7.1	0.32	2992	2974	−0.97
14	2825	0.001208	0.032439	0.281190	0.000009	0.281124	5.3	0.32	2891	2929	−0.96
15	2831	0.000999	0.025886	0.280978	0.000018	0.280924	−1.7	0.64	3162	3360	−0.97
16	2776	0.001354	0.034484	0.281258	0.000008	0.281185	6.3	0.27	2809	2828	−0.96
18	2892	0.000562	0.014694	0.281084	0.000008	0.281053	4.3	0.27	2984	3041	−0.98
19	2815	0.001643	0.041108	0.281212	0.000010	0.281123	5.0	0.35	2894	2939	−0.95
21	2820	0.001725	0.047275	0.281269	0.000015	0.281176	7.0	0.52	2821	2821	−0.95
23	2729	0.001474	0.036317	0.281232	0.000012	0.281155	4.1	0.43	2853	2925	−0.96
24	2729	0.001028	0.026517	0.281146	0.000010	0.281093	1.9	0.34	2936	3060	−0.97
25	2883	0.001461	0.037563	0.281187	0.000009	0.281106	6.0	0.31	2914	2931	−0.96
14WG-3 (BIF)											
1	2661	0.000468	0.010334	0.281063	0.000015	0.281039	−1.5	0.53	3006	3220	−0.99
2	2696	0.000670	0.016644	0.281228	0.000011	0.281193	4.7	0.38	2800	2863	−0.98
3	2789	0.000425	0.010183	0.281042	0.000013	0.281020	0.7	0.45	3030	3180	−0.99
4	2672	0.000568	0.014005	0.281199	0.000027	0.281170	3.4	0.96	2830	2928	−0.98
6	2757	0.001085	0.026860	0.281193	0.000014	0.281136	4.1	0.49	2877	2948	−0.97

[a] Initial Hf isotopic compositions.

detritus at these surroundings. Furthermore, the ferrous Fe in shallow water can be transport into deep water by oxidation, precipitation and deposition. These features need a depositional environment more proximal to the palaeo shoreline, most likely on the shelf slope or back-arc basin.

6.4. Comparison with other BIFs in the NCC

The Wugang BIF displayed many similarities with the Huoqiu BIF, which is located at 300 km in its southeast direction. The age of the Huoqiu BIF deposition was constrained at Neoarchean by zircons U-Pb dating (Wang et al., 2014; Liu and Yang, 2015). They proposed that Huoqiu complex lacked later Neoarchean volcanic activity, despite Wan et al. (2010) dated a granitoid at 2.56 Ga in this area. Similarly, later Neoarchean volcanic events have rarely been reported from the Wugang unit, and previous geologists have also noted this feature (e.g., Wan et al., 2006; Diwu et al., 2010; Shen and Song, 2014), which is also reflected in age distribution diagram of detrital zircons from TSM (Fig. 8a). The lack of volcanic activity must lead to absence of coeval BIF. In contrast, most BIFs from northern NCC were formed at 2.56–2.52 Ga as a result of intensive and extensive coeval volcanic activity (Zhang et al., 2012 and references therein).

The BIFs from northern NCC are closely associated with volcanic rocks, and formed in arc/back-arc basins, consequently, large amounts of BIFs are regarded as Algoma-type, e.g., Eastern Hebei, Anshan-Benxi iron deposits. However, the associated rocks with the Wugang and Huoqiu BIFs are mainly composed of marble, schist, quartzite and paragneiss. No or minor volcanic materials can be found, but great

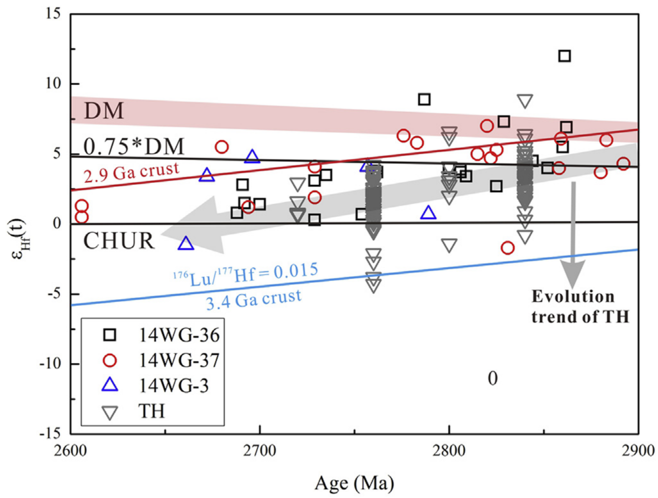

Fig. 10. Plots of $\varepsilon_{Hf}(t)$ versus $^{207}Pb/^{206}Pb$ ages of all detrital zircons from samples 14WG-36, 14WG-37 and 14WG-3. CHUR: Chondrite Uniform Reservoir, DM: Depleted Mantle. TH: the Hf isotope and age data of TTG rocks from Taihua complex are sourced from previous references (Liu et al., 2009; Huang et al., 2010; Diwu et al., 2010; Zhou et al., 2014; Jia et al., 2016). 0.75 time $\varepsilon_{Hf}(t)$ of DM referred to Belousova et al. (2010), which is used to judge whether or not the juvenile crust is. Light grey arrow denotes the 2.9 Ga juvenile crust evolutional direction within TH.

amounts of Fe-rich carbonate minerals, such as siderite, ankerite and breunnerite, occurred in the ore. Indeed, the magmatic detrital zircons in BIF samples and their associated paragneisses may be derived from the coeval volcanic activity. However, their characteristics are in good agreement with those zircons from basement rocks (the features of zircons from basement rocks see in Liu and Yang (in press) for detail), with respect to REE and Hf isotopes (Figs. 9 and 10). Weakly rounded shape in zircon CL image suggests they have been transported a short distance. Moreover, the oscillatory zoning features in zircon core domain are similar to those from basement rocks, e.g., TTG gneisses. The consistent age and Lu-Hf isotopic characteristics between each other, confirm their affiliation. Therefore, we exclude the coeval volcanic activity as the source of these detrital zircons. The volcanic activity at this time around this area has not been reported until now. On the basis of the depositional environment (continental margin or back-arc basin) of both Wugang and Huoqiu BIF, they have been referred to Superior-type, which is commonly regarded as banding or flaky. Thus it is reasonable to infer that a great variety of Superior-type BIF orebodies may distribute between Wugang and Huoqiu area at the southern margin of NCC. Recently, the Xincai BIF, located between Wugang and Huoqiu area, has been dated at 2.5–2.7 Ga, and identified the depositional environment similar to Huoqiu BIF (Lan et al., 2017a). This report further supports the metallogenic prognosis in this study.

7. Conclusions

The Wugang BIF, located in Henan Province, is closely associated with supracrustal rocks (dominated by metasedimentary rocks) of TSM, composing mainly of early Neoarchean basement rocks, such as TTG gneisses and amphibolites. Detrital zircons U-Pb dating give an age constraint at 2.60–2.45 Ga, where the lower limit age is determined by the maximum metamorphic age peak of the Wugang BIF sample suffered. The occurrence of proximal detrital zircons, carbonate rocks as the major hosting rock, and the presence of abundant carbonate minerals in BIF sample suggest the Wugang BIF belongs to Superior-type, furthermore, the geochemical characteristics of Eu and Ce anomalies consolidate this viewpoint. Consequently, the Wugang BIF deposited in near-shore continental-shelf or back-arc basin environments. In term of the similarity in depositional environment and time between the Wugang and Huoqiu BIF, it can predict that a great variety of Superior-type BIF orebodies may distribute between Wugang and Huoqiu area at the southern margin of NCC.

Acknowledgements

The authors are grateful to two anonymous reviewers and Editor-in-Chief Prof. Franco Pirajno for their helpful comments and suggestions that greatly helped to improve an earlier manuscript version. We particularly thank Editor Dr. Paul Duuring for the complete English revision of the manuscript. We appreciate H. Zhang, M.L. Dai, Z.H. Hou, M. Xia, J.H. Deng, H.L. Gu, H.S. Qi, Y.S. Ren, X. Zhang, S.Y. Shu, and Q. Hu for assistance in zircon U-Pb dating and Lu-Hf isotope analyses. Finally, we greatly thank Prof. Y.Y. Zhang and X.X. Lu, and Z.L. Hu and Y.Q. Duan for field assistance. The research was supported by Natural Science Foundation of China (41603003) and State Key Basic Research Development Program of China (2012CB416602).

Appendix A. Supplementary data

Supplementary data associated with this article can be found, in the online version, at http://dx.doi.org/10.1016/j.oregeorev.2018.04.005.

References

Alexander, B.W., Bau, M., Andersson, P., Dulski, P., 2008. Continentally-derived solutes in shallow Archean seawater: rare earth element and Nd isotope evidence in iron formation from the 2.9 Ga Pongola Supergroup, South Africa. Geochim. Cosmochim. Acta 72, 378–394.
Alexander, B.W., Bau, M., Andersson, P., 2009. Neodymium isotopes in Archean seawater and implications for the marine Nd cycle in Earth's early oceans. Earth Planet. Sci. Lett. 283, 144–155.
Alibo, D.S., Nozaki, Y., 1999. Rare earth elements in seawater: Particle association, shale-normalization, and Ce oxidation. Geochim. Cosmochim. Acta 63, 363–372.
Baker, J., Peate, D., Waight, T., Meyzen, C., 2004. Pb isotopic analysis of standards and samples using a Pb-207-Pb-204 double spike and thallium to correct for mass bias with a double-focusing MC-ICP-MS. Chem. Geol. 211, 275–303.
Bau, M., Möller, P., 1993. Rare earth element systematics of the chemically precipitated component in early Precambrian iron formations and the evolution of the terrestrial atmosphere-hydrosphere-lithosphere system. Geochim. Cosmochim. Acta 57 (10), 2239–2249.
Bau, M., Dulski, P., 1996. Distribution of yttrium and rare-earth elements in the Penge and Kuruman iron-formations, Transvaal Supergroup, South Africa. Precambr. Res. 79, 37–55.
Bau, M., Dulski, P., 1999. Comparing yttrium and rare earths in hydrothermal fluids from the Mid-Atlantic Ridge: implications for Y and REE behaviour during near-vent mixing and for the Y/Ho ratio of Proterozoic seawater. Chem. Geol. 155, 77–90.
Bekker, A., Slack, J.F., Planavsky, N., Krapež, B., Hofmann, A., Konhauser, K.O., Rouxel, O.J., 2010. Iron Formation: The Sedimentary Product of a Complex Interplay among Mantle, Tectonic, Oceanic, and Biospheric Processes. Econ. Geol. 105, 467–508.
Belousova, E.A., Kobayashi, K.L., Griffin, W.L., Begg, G.S., O'Reilly, S.Y., Pearson, D.G., 2010. The growth of the continental crust: constraints from zircon Hf-isotope data. Lithos 119 (3–4), 457–466.
Blichert-Toft, J., Albarede, F., 1997. The Lu-Hf isotope geochemistry of chondrites and the evolution of the mantle–crust system. Earth Planet. Sci. Lett. 148, 243–258.
Bolhar, R., Kamber, B.S., Moorbath, S., Fedo, C.M., Whitehouse, M.J., 2004. Characterisation of early Archaean chemical sediments by trace element signatures. Earth Planet. Sci. Lett. 222, 43–60.
Cabral, A.R., Lehmann, B., Gomes Jr, A.A.S., Pašava, J., 2016. Episodic negative anomalies of cerium at the depositional onset of the 2.65-Ga Itabira iron formation, Quadrilátero Ferrífero of Minas Gerais, Brazil. Precambrian Res. 276, 101–109.
Chu, N.C., Taylor, R.N., Chavagnac, V., Nesbitt, R.W., Boella, R.M., Milton, J.A., Germain, C.R., Bayon, G., Burton, K., 2002. Hf isotope ratio analysis using multi-collector inductively coupled plasma mass spectrometry: an evaluation of isobaric interference corrections. J. Anal. At. Spectrom. 17, 1567–1574.
Cloud, P., 1973. Paleoecological significance of the banded iron-formation. Econ. Geol. 68 (7), 1135–1143.
Delvigne, C., Cardinal, D., Hofmann, A., André, L., 2012. Stratigraphic changes of Ge/Si, REE + Y and silicon isotopes as insights into the deposition of a Mesoarchean banded iron formation. Earth Planet. Sci. Lett. 355–366, 109–118.
Derry, L.A., Jacobsen, S.B., 1990. The chemical evolution of Precambrian seawater: Evidence from REEs in banded iron formations. Geochim. Cosmochim. Acta 54, 2965–2977.
Diwu, C., Sun, Y., Lin, C., Wang, H., 2010. LA-(MC)-ICPMS U-Pb zircon geochronology and Lu-Hf isotope compositions of the Taihua Complex on the southern margin of the North China Craton. Chin. Sci. Bull. 55 (21), 2112–2123 (in Chinese with English abstract).
Fantle, M.S., DePaolo, D.J., 2004. Iron isotopic fractionation during continental

weathering. Earth Planet. Sci. Lett. 228 (3–4), 547–562.
Frei, R., Polat, A., 2007. Source heterogeneity for the major components of ∼3.7 Ga Banded Iron Formations (Isua Greenstone Belt, Western Greenland): Tracing the nature of interacting water masses in BIF formation. Earth Planet. Sci. Lett. 253, 266–281.
Frost, B.R., Chamberlain, K.R., Schumacher, J.C., 2001. Sphene (titanite): phase relations and role as a geochronometer. Chem. Geol. 172, 131–148.
Griffin, W.L., Pearson, N.J., Belousova, E., Jackson, S.E., van Achterbergh, E., O'Reilly, S.Y., Shee, S.R., 2000. The Hf isotope composition of cratonic mantle: LAM-MC-ICP-MS analysis of zircon megacrysts in kimberlites. Geochim. Cosmochim. Acta 64, 133–147.
Griffin, W.L., Wang, X., Jackson, S.E., Pearson, N.J., O'Reilly, S.Y., Xu, X.S., Zhou, X.M., 2002. Zircon chemistry and magma mixing, SE China: in situ analysis of Hf isotopes, Tonglu and Pingtan igneous complexes. Lithos 61, 237–269.
Gross, G.A., 1980. A classification of iron-formation based on depositional environments. Can. Mineral. 18, 215–222.
Hanchar, J.M., Rundnick, R.L., 1995. Revealing hidden structures: the application of cathodolum- inescene and back-scattered electron imaging to dating zircons from lower crustal xenoliths. Lithos 36, 289–303.
Haugaard, R., Frei, R., Stendal, H., Konhauser, K., 2013. Petrology and geochemistry of the ∼2.9Ga Itilliarsuk banded iron formation and associated supracrustal rocks, West Greenland: Source characteristics and depositional environment. Precambr. Res. 229, 150–176.
Holland, H.D., 1984. The chemical evolution of the Atmosphere and oceans. Princeton University Press, Princeton.
Huang, X.-L., Niu, Y., Xu, Y.-G., Yang, Q.-J., Zhong, J.-W., 2010. Geochemistry of TTG and TTG-like gneisses from Lushan-Taihua complex in the southern North China Craton: Implications for late Archean crustal accretion. Precambr. Res. 182 (1–2), 43–56.
Huston, D.L., Logan, G.A., 2004. Barite, BIFs and bugs: evidence for the evolution of the Earth's early hydrosphere. Earth Planet. Sci. Lett. 220, 41–55.
James, H.L., 1992. Precambrian iron-formations: nature, origin, and mineralogic evolution from sedimentation to metamorphism. In: Wolf, K.H., Chilingarian, G.V. (Eds.), Diagensis III. Developments in Sedimentology, pp. 543–589.
Jia, X., et al., 2016. Late Mesoarchean crust growth event: evidence from the ca. 2.8 Ga granodioritic gneisses of the Xiaoqinling area, southern North China Craton. Science Bulletin 61 (12), 974–990.
Kato, Y., Kawakami, T., Kano, T., Kunugiza, K., Swamy, N.S., 1996. Rare-earth element geochemistry of banded iron formations and associated amphibolite from the Sargur belts, south India. J. SE Asian Earth Sci. 14, 161–164.
Khan, R.M.K., Das Sharma, S., Patil, D.J., Naqvi, S.M., 1996. Trace, rare-earth element, and oxygen isotopic systematics for the genesis of banded iron-formations: evidence fromthe Kushtagi schist belt, Archaean Dharwar Craton. India. Geochim. Cosmochim. Acta 60, 3285–3294.
Klein, C., 2005. Some Precambrian banded iron-formations (BIFs) from around the world: Their age, geologic setting, mineralogy, metamorphism, geochemistry, and origin. Am. Mineral. 90, 1473–1499.
Klemme, S., Guenther, D., Hametner, K., Prowatke, S., Zack, T., 2006. The partitioning of trace elements between ilmenite, ulvospinel, annalcolite and silicate melts with implications for the early differentiation of the moon. Chem. Geol. 234, 251–263.
Kramers, J.D., 2002. Global modeling of continent formation and destruction through geological time and implications for CO_2 drawdown in the Archaean Eon. In: In: Fowler, C.M.R., Ebinger, C.J., Hawkesworth, C.J. (Eds.), The Early Earth: Physical, Chemical and Biological Development, vol. 199. The Geological Society, London, pp. 259–274.
Kröner, A., Compston, W., Guo-wei, Z., An-lin, G., Todt, W., 1988. Age and tectonic setting of Late Archean greenstone-gneiss terrain in Henan Province, China, as revealed by single-grain zircon dating. Geology 16, 211–215.
Lan, C.Y., Zhang, L.C., Zhao, T.P., Wang, C.L., Li, H.Z., Zhou, Y.Y., 2013. Mineral and geochemical characteristics of the Tieshanmiao-type BIF-iron deposit in Wuyang region of Henan Province and its implications for ore-forming process. Acta Petrol. Sin. 29, 2567–2582 (in Chinese with English abstract).
Lan, C.Y., Zhao, T.P., Luo, Z.Z., Wang, C.L., Wen, Q.F., Liu, L.X., 2015. The genesis of the Zhaoanzhuang Fe oxide deposit in Wuyang region of Henan Province: Insights from magnetite and apatite. Acta Petrol. Sin. 29, 2567–2582 (in Chinese with English abstract).
Lan, C., Yang, A.Y., Wang, C., Zhao, T., 2017a. Geochemistry, U-Pb zircon geochronology and Sm-Nd isotopes of the Xincai banded iron formation in the southern margin of the North China Craton: Implications on Neoarchean seawater compositions and solute sources. Precambr. Res. http://dx.doi.org/10.1016/j.precamres.2017.10.024.
Lan, C., Zhou, Y., Wang, C., Zhao, T., 2017b. Depositional age and protoliths of the Paleoproterozoic upper Taihua Group in the Wuyang area in the southern margin of the North China Craton: New insights into stratigraphic subdivision and tectonic setting. Precambr. Res. 297, 77–100.
Lan, T.G., Fan, H.R., Santosh, M., Hu, F.F., Yang, K.F., Liu, Y.S., 2014. U-Pb zircon chronology, geochemistry and isotopes of the Changyi banded iron formation in the eastern Shandong Province: Constraints on BIF genesis and implications for Paleoproterozoic tectonic evolution of the North China Craton. Ore Geol. Rev. 56, 472–486.
Lepp, H., Goldich, S., 1964. Origin of Precambrian iron formations. Econ. Geol. 59 (6), 1025–1060.
Li, H., Zhai, M., Zhang, L., Yang, Z., Kapsiotis, A., Zhou, Y., He, J., Wang, C., Liang, J., 2014. Mineralogical and microfabric characteristics of magnetite in the Wuyang Precambrian BIFs, southern North China Craton: Implications for genesis and depositional processes of the associated BIFs. J. Asian Earth Sci. 94, 267–281.
Li, W., Beard, B.L., Johnson, C.M., 2015. Biologically recycled continental iron is a major component in banded iron formations. Proc. Natl. Acad. Sci. 112, 8193–8198.
Li, Y.F., Xie, K., Luo, Z., Li, J., 2013. Geochemistry of Tieshan iron deposit in the Wuyang Area, Henan Province and its environmental implications. Acta Geol. Sin. 87 (9), 1377–1398 (in Chinese with English abstract).
Li, Y.H., Hou, K., Wan, D., Zhang, Z., 2012. A compare geochemistry study for Algoma- and Superior-type banded iron formations. Acta Petrological Sinica 28 (11), 3513–3519 (in Chinese with English abstract).
Liu, D.Y., Wilde, S.A., Wan, Y., Wang, S., Valley, J.W., Kita, N., Dong, C., Xie, H., Yang, C., Zhang, Y., Gao, L., 2009. Combined U-Pb, hafnium and oxygen isotope analysis of zircons from meta-igneous rocks in the southern North China Craton reveal multiple events in the Late Mesoarchean-Early Neoarchean. Chem. Geol. 261, 140–154.
Liu, L., Yang, X., 2015. Temporal, environmental and tectonic significance of the Huoqiu BIF, southeastern North China Craton: Geochemical and geochronological constraints. Precambr. Res. 261, 217–233.
Liu, L., Yang, X., Santosh, M., Zhao, G., Aulbach, S., 2016. U-Pb age and Hf isotopes of detrital zircons from the Southeastern North China Craton: Meso- to Neoarchean episodic crustal growth in a shifting tectonic regime. Gondwana Res. 35, 1–14.
Liu, L., Yang, X., Crust periodic evolution: evidence from the Taihua complex, southern North China Craton. Precambrian Research. https://doi.org/10.1016/j.precamres.2017.12.034 (in press).
Liu, Q., Li, Y., Luo, Z., Xie, K., Huang, Z., 2014. Geochemical characteristics of Jingshansi iron deposit in Wuyang, Henan Province, and their geological significance. Miner. Deposita 33 (4), 697–712 (in Chinese with English abstract).
Liu, X., Gao, S., Diwu, C.-R., Yuan, H., Hu, Z., 2007. Simultaneous in-site determination of U-Pb age and trace elements in zircon by LA-ICP-MS in 20 µm spot size. Chin. Sci. Bull. 52, 1257–1264.
Lu, J.-S., Wang, G.-D., Wang, H., Chen, H.-X., Wu, C.-M., 2013. Metamorphic P-T-t paths retrieved from the amphibolites, Lushan terrane, Henan Province and reappraisal of the Paleoproterozoic tectonic evolution of the Trans-North China Orogen. Precambr. Res. 238, 61–77.
Lu, J.-S., Wang, G.-D., Wang, H., Chen, H.-X., Wu, C.-M., 2014. Palaeoproterozoic metamorphic evolution and geochronology of the Wugang block, southeastern terminal of the Trans-North China Orogen. Precambr. Res. 251, 197–211.
Lu, J.-S., Zhai, M.G., Lu, L.S., Wang, H.Y.C., Chen, H.X., Peng, T., Wu, C.M., Zhao, T.P., 2017. Metamorphic P-T-t path retrieved from metapelites in the southeastern Taihua metamorphic complex, and the Paleoproterozoic tectonic evolution of the southern North China Craton. J. Asian Earth Sci. 134, 352–364.
Ludwig, K.R., 2003. In: ISOPLOT 3: A Geochronological Toolkit for Microsoft Excel. Berkeley Geochronology Center Special Publication, pp. 74.
Luo, M.Q., 2009. Study on ore-controlling factors in Wuyang iron ore field in Henan province (in Chinese with English abstract). J. Henan Polytech. Univ. (Nat. Sci.) 28 (5), 576–582.
Machado, N., Simonetti, A., 2001. U-Pb dating and Hf isotopic composition of zircon by laser ablation MC-ICP-MS. In: Sylvester, P. (Ed.), Laser-Ablation-ICPMS in the Earth Sciences: Principles and Applications. Short Course of Mineralogical Association of Canada, pp. 29.
McLennan, S.M., 1989. Rare earth elements in sedimentary rocks; influence of provenance and sedimentary processes. Rev. Mineral. Geochem. 21 (1), 169–200.
Nowell, G.M., Kempton, P.D., Noble, S.R., Fitton, J.G., Saunders, A.D., Mahoney, J.J., Taylor, R.N., 1998. High precision Hf isotope measurements of MORB and OIB by thermal ionisation mass spectrometry: insights into the depleted mantle. Chem. Geol. 149, 211–233.
Nozaki, Y., Zhang, J., Amakawa, H., 1997. The fractionation between Y and Ho in the marine environment. Earth Planet. Sci. Lett. 148, 329–340.
Planavsky, N., Bekker, A., Rouxel, O.J., Kamber, B., Hofmann, A., Knudsen, A., Lyons, T.W., 2010. Rare Earth Element and yttrium compositions of Archean and Paleoproterozoic Fe formations revisited: new perspectives on the significance and mechanisms of deposition. Geochim. Cosmochim. Acta 74, 6387–6405.
Rudnick, R.L., Gao, S., 2003. Composition of the continental crust. In: Rudnick, R.L. (Ed.), The Crust. Treatise in Geochemistry, pp. 1–64.
Scherer, E., Münker, C., Mezger, K., 2001. Calibration of the lutetium-hafnium clock. Science 293, 683–687.
Schimmelmann, A., Lange, C.B., Schieber, J., Francus, P., Ojala, A.E.K., Zolitschka, B., 2016. Varves in marine sediments: A review. Earth Sci. Rev. 159, 215–246.
Shen, Q.H., Song, H.X., 2014. Rederinition of the Taihua Group, Lushan, Henan. J. Stratigr. 38 (1), 1–7 (in Chinese with English abstract).
Sun, S.S., McDonough, W.F., 1989. In: Chemical and isotopic systematics of oceanic basalts: implications for mantle composition and processes. Geological Society, London, pp. 313–345.
Trendall, A.F., 2002. The significance of iron-formation in the Precambrian stratigraphic record. Spec. Publ. Int. Assoc. Sedimentol. 33, 33–66.
Trendall, A.F., Blockley, J.G., 1970. The iron formations of the Precambrian Hamersley group, Western Australia. Geol. Survey West. Aust. Bull. 119, 366.
Wan, Y.S., Wilde, S.A., Liu, D., Yang, C., Song, B., Yin, X., 2006. Further evidence for ∼1.85 Ga metamorphism in the Central Zone of the North China Craton: SHRIMP U-Pb dating of zircon from metamorphic rocks in the Lushan area, Henan Province. Gondwana Res. 9, 189–197.
Wan, Y.S., Liu, D.Y., Wang, S.Y., Zhao, X., Dong, C.Y., Zhou, H.Y., Yin, X.Y., Yang, C.X., Gao, L.Z., 2009. Early Precambrian crustal evolution in the Dengfeng area, Henan Province (eastern China): Constraints from geochemistry and SHRIMP U-Pb zircon dating. Acta Geol. Sin. 83 (7), 982–999 (in Chinese with English abstract).
Wan, Y.S., Dong, C.Y., Wang, W., Xie, H.Q., Liu, D.Y., 2010. Archean Basement and a Paleoproterozoic Collision Orogen in the Huoqiu Area at the Southeastern Margin of North China Craton: Evidence from Sensitive High Resolution Ion Micro-Probe U-Pb Zircon Geochronology. Acta Geol. Sin. Engl. Ed. 84, 91–104.
Wang, C., Wu, H., Li, W., Peng, Z., Zhang, L., Zhai, M., 2017. Changes of Ge/Si, REE + Y and SmNd isotopes in alternating Fe- and Si-rich mesobands reveal source

heterogeneity of the ~2.54 Ga Sijiaying banded iron formation in Eastern Hebei, China. Ore Geol. Rev. 80, 363–376.
Wang, G.C., Cao, P., Zhang, Q.L., Chen, J.F., 2006. Formation of the Tieshanmiao-type iron deposits in Henan province and research on the characteristics of oxidation of the "ERTIE" deposit. Acta Mineral. Sinica 26 (4), 431–434 (in Chinese with English abstract).
Wang, H., Kang, J., Ren, Y., Chu, H., Lu, S., Xiao, Z., 2015. Identification of ~2.7 Ga BIF in North China Craton: Evidence from geochronology of iron-bearing formation in Laizhou-Changyi area, Jiaobei terrane. Acta Petrol. Sin. 31 (10), 2991–3011 (in Chinese with English abstract).
Wang, Q.Y., Zheng, J.P., Pan, Y., Dong, Y., Liao, F., Zhang, Y., Zhang, L., Zhao, G., Tu, Z., 2014. Archean crustal evolution in the southeastern North China Craton: new data from the Huoqiu Complex. Precambr. Res. 255, 294–315.
Watson, E.B., Wark, D.A., Thomas, J.B., 2006. Crystallization thermometers for zircon and rutile. Contrib. Miner. Petrol. 151, 413–433.
Xie, S., Xie, H., Liu, S., Dong, C., 2016. Archean crustal formation and evolution of the Lushan area in the souther margin of the North China Craton. Geol. China 43 (6), 1884–1890 (in Chinese with English abstract).
Xu, X., Griffin, W., Ma, X., O'Reilly, S., He, Z., Zhang, C., 2009. The Taihua group on the southern margin of the North China craton: further insights from U-Pb ages and Hf isotope compositions of zircons. Miner. Petrol. 97, 43–59.
Xue, L.W., Yuan, Z.L., Zhang, Y.S., Qiang, L.Z., 1995. The Sm–Nd isotope age of Taihua Group in the Lushan area and their implications. Geochimica 24 (Suppl.), 92–97 (in Chinese with English abstract).
Yamaguchi, K.E., Johnson, C.M., Beard, B.L., Ohmoto, H., 2005. Biogeochemical cycling of iron in the Archean-Paleoproterozoic Earth: constraints from iron isotope variations in sedimentary rocks from the Kaapvaal and Pilbara Cratons. Chem. Geol. 218, 135–169.
Yang, C.X., Wang, S.Y., Liu, Z.H., Lei, Z.H., Yang, C.Q., 2008. Mesoarchean-Neoarchean grey gneiss in the Lushan area, Henan Province. Geol. Rev. 54 (3), 327–334 (in Chinese with English abstract).
Yao, T., Li, H.M., Li, W.J., Li, L.X., Zhao, C., 2015. Origin of the disseminated magnetite pyroxenite in the Tieshanmiao-type iron deposits in the Wuyang region of Henan Province, China. J. Asian Earth Sci. 113, 1235–1252.
Yu, S.J., Liang, Y.H., Du, S.H., Li, S.Z., Liu, K.J., 1981. Research in ore-forming geological characteristic and configuration of iron-bearing basin of Tieshanmiao-type iron deposits of Late Archaean in the central Henan and western Anhui. J. Yichang Inst. Geol. Miner. Resour. Chin. Acad. Geol. Sci. 3, 68–83 (in Chinese with English abstract).
Yuan, H.-L., Gao, S., Dai, M.-N., Zong, C.-L., Günther, D., Fontaine, G.H., Liu, X.-M., Diwu, C., 2008. Simultaneous determinations of U-Pb age, Hf isotopes and trace element compositions of zircon by excimer laser-ablation quadrupole and multiple-collector ICP-MS. Chem. Geol. 247, 100–118.
Zack, T., Krönz, A., Foley, S.F., Rivers, T., 2002. Trace element abundances in rutiles from eclogites and associated garnet mica schists. Chem. Geol. 184, 97–122.
Zhai, M.G., Santosh, M., 2011. The early Precambrian odyssey of the North China Craton: a synoptic overview. Gondwana Res. 20 (1), 6–25.
Zhai, M.G., Santosh, M., 2013. Metallogeny of the North China Craton: Link with secular changes in the evolving Earth. Gondwana Res. 24 (1), 275–297.
Zhang, H., Wang, J., Zhou, D., Yang, Y., Zhang, G., Santosh, M., Yu, H., Zhang, J., 2014. Hadean to Neoarchean episodic crustal growth: Detrital zircon records in Paleoproterozoic quartzites from the southern North China Craton. Precambr. Res. 254, 245–257.
Zhang, K., Shen, B., Sun, F., Zhou, H., Li, H., 2016. Metallogenic epoch of Zhaoanzhuang iron ore deposit in Wuyang, Henan Province: oldest magmatic type iron ore deposit in China. Miner. Deposita 35 (5), 889–901 (in Chinese with English abstract).
Zhang, L.C., Zhai, M.G., Wan, Y.S., Guo, J.H., Dai, Y.P., Wang, C.L., Liu, L., 2012. Study of the Precambrian BIF-iron deposits in the North China Craton: Progresses and questions. Acta Petrol. Sin. 28, 3431–3445 (in Chinese with English abstract).
Zhao, G., Sun, M., Wilde, S.A., Li, S., 2005. Late Archean to Paleoproterozoic evolution of the North China Craton: key issues revisited. Precambr. Res. 136 (2), 177–202.
Zhao, G., Zhai, M., 2013. Lithotectonic elements of Precambrian basement in the North China Craton: Review and tectonic implications. Gondwana Res. 23 (4), 1207–1240.
Zhou, Y.Y., Zhao, T.-P., Wang, C.Y., Hu, G.-H., 2011. Geochronology and geochemistry of 2.5 to 2.4 Ga granitic plutons from the southern margin of the North China Craton: Implications for a tectonic transition from arc to post-collisional setting. Gondwana Res. 20, 171–183.
Zhou, Y.Y., Zhao, T.P., Zhai, M.G., Gao, J.F., Sun, Q.Y., 2014. Petrogenesis of the Archean tonalite-trondhjemite-granodiorite (TTG) and granites in the Lushan area, southern margin of the North China Craton: Implications for crustal accretion and transformation. Precambr. Res. 255, 514–537.
Zhou, Y.Y., Zhao, T.-P., Zhai, M.-G., Gao, J.-F., Lan, Z.-W., Sun, Q.-Y., 2015. Petrogenesis of the 2.1Ga Lushan garnet-bearing quartz monzonite on the southern margin of the North China Craton and its tectonic implications. Precambr. Res. 256, 241–255.